# Implementing RapidArc into clinical routine: A comprehensive program from machine QA to TPS validation and patient QA

Ann Van Esch and Dominique P. Huyskens
*7Sigma, QA-team in Radiotherapy Physics, 3150 Tildonk, Belgium and Department of Radiotherapy, Clinique Ste. Elisabeth, 5000 Namur, Belgium*

Claus F. Behrens, Eva Samsøe, Maria Sjölin, Ulf Bjelkengren, and David Sjöström
*Department of Oncology, Division of Radiophysics, Copenhagen University Hospital, 2730 Herlev, Denmark*

Christian Clermont, Lionel Hambach, and François Sergent
*Department of Radiotherapy, Clinique Ste. Elisabeth, 5000 Namur, Belgium*

(Received 27 March 2011; revised 20 June 2011; accepted for publication 15 July 2011; published 24 August 2011)

**Purpose:** With the increased commercial availability of intensity modulated arc therapy (IMAT) comes the need for comprehensive QA programs, covering the different aspects of this newly available technology. This manuscript proposes such a program for the RapidArc (RA) (Varian Medical Systems, Palo Alto) IMAT solution.
**Methods:** The program was developed and tested out for a Millennium120 MLC on iX Clinacs and a HighDefinition MLC on a Novalis TX, using a variety of measurement equipment including Gafchromic film, 2D ion chamber arrays (Seven29 and StarCheck, PTW, Freiburg, Germany) with inclinometer and Octavius phantom, the Delta4 systam (ScandiDos, Uppsala, Sweden) and the portal imager (EPID). First, a number of complementary machine QA tests were developed to monitor the correct interplay between the accelerating/decelerating gantry, the variable dose rate and the MLC position, straining the delivery to the maximum allowed limits. Second, a systematic approach to the validation of the dose calculation for RA was adopted, starting with static gantry and RA specific static MLC shapes and gradually moving to dynamic gantry, dynamic MLC shapes. RA plans were then optimized on a series of artificial structures created within the homogeneous Octavius phantom and within a heterogeneous lung phantom. These served the double purpose of testing the behavior of the optimization algorithm (PRO) as well as the precision of the forward dose calculation. Finally, patient QA on a series of clinical cases was performed with different methods. In addition to the well established in-phantom QA, we evaluated the portal dosimetry solution within the Varian approach.
**Results:** For routine machine QA, the "Snooker Cue" test on the EPID proved to be the most sensitive to overall problem detection. It is also the most practical one. The "Twinkle" and "Sunrise" tests were useful to obtain well differentiated information on the individual treatment delivery components. The AAA8.9 dose calculations showed excellent agreement with all corresponding measurements, except in areas where the 2.5 mm fixed fluence resolution was insufficient to accurately model the tongue and groove effect or the dose through nearly closed opposing leafs. Such cases benefited from the increased fluence resolution in AAA10.0. In the clinical RA fields, these effects were smeared out spatially and the impact of the fluence resolution was considerably less pronounced. The RA plans on the artificial structure sets demonstrated some interesting characteristics of the PRO8.9 optimizer, such as a sometimes unexpected dependence on the collimator rotation and a suboptimal coverage of targets within lung tissue. Although the portal dosimetry was successfully validated, we are reluctant to use it as a sole means of patient QA as long as no gantry angle information is embedded.
**Conclusions:** The all-in validation program allows a systematic approach in monitoring the different levels of RA treatments. With the systematic approach comes a better understanding of both the capabilities and the limits of the used solution. The program can be useful for implementation, but also for the validation of major upgrades.  [DOI: 10.1118/1.3622672]

## I. INTRODUCTION

Following Yu *et al.*[1] we use intensity-modulated arc therapy (IMAT) as a generic term to denote radiation therapy delivery based on a rotating intensity modulated cone beam. For IMAT, the MLC moves during beam-on as for dynamic IMRT. However, the intensity–modulation may also be partly accomplished by varying the dose rate, gantry speed, and possibly even the collimator angle. The first stepping stones for IMAT were laid down many decades ago. For an extensive topical review, we refer to the publication by Yu *et al.*[1] and the references mentioned therein. The widespread

implementation of the technique in clinical practice has only begun in the recent years because the major vendors of medical linear accelerator vendors have only recently begun to commercialize integrated IMAT solutions. These commercial implementations of IMAT are—at least partly—based on or facilitated by the work published by the different pioneering groups (for a detailed overview, again see Yu *et al.*[1] and Refs. 2–5).

As IMAT is a more complicated technique than IMRT in terms of treatment planning and delivery, the standard QA and commissioning procedures used for IMRT are not sufficient. For instance, IMAT beams may encompass more complicated MLC movements than usually seen for IMRT, including small MLC openings in large collimator openings and single MLC leaves sticking out into the beam. Thus, models and model parameters for the MLC transmission, tongue and groove, and rounded leaf ends that suffice for IMRT may be insufficient for IMAT. The optimization algorithm and possibly also the dose calculation engine differs for IMAT and requires separate commissioning and QA. Additionally, extra strain is put on the treatment machine performance because of, e.g., variable gantry speed and gantry angle dependent dose rate modulation. For these reasons, IMAT specific QA programs must be developed to ensure that the planned dose distributions correspond to the delivered ones and to ensure reliable, stable and reproducible delivery.[6–9] Naturally, the QA procedures needed for IMAT depend on the chosen IMAT solution. Designing a proper QA and commissioning program for IMAT requires knowledge and understanding of how the IMAT solution is constructed and how the different parts interact. In this work we focus on the Varian implementation of IMAT called RapidArc (RA), using both the Varian treatment planning system (TPS) and the Varian linear accelerators. RapidArc treatment plan optimization in the Eclipse TPS is based on the work of Otto *et al.*[10]

In most cases, a RA delivery utilizes fewer monitor units (MUs) and is considerably faster than the corresponding dynamic IMRT treatment plan while preserving treatment plan quality (see, e.g., the review published by Palma *et al.*[4] and the references mentioned therein). Shorter treatment times have obvious advantages including better patient throughput, improved patient comfort and, possibly, less intra fractional motion. Thus, a demand for a clinical implementation of RA is justified. For a Clinac to be RA compatible, it requires the appropriate controller software. Additionally, a separate RA license on the TPS side is mandatory. RA was originally advertised as a one arc technique. However, even though one arc is sufficient for a number of cases (e.g., prostate), two arcs are usually required for more complex cases (e.g., head and neck).[11–15] Multiple arc solutions are now fully supported by the system (Eclipse version beyond 8.9). QA for RA is often comprised of machine, TPS, and patient specific QA. For the latter, the patient specific treatment plan is usually recalculated on and delivered to a phantom containing some dose detectors, e.g., ionization chambers, diodes, or film. In addition, portal dosimetry and independent dose calculations can be employed. There have been several publications on patient specific QA (Refs. 16–26) and numerous planning studies including comparisons of RA, IMRT, tomotherapy, and particle therapy.[26–47] However, when it comes to designing a comprehensive QA and commissioning program including machine QA only little has been published.[6,7] Ling *et al.*[6] have published the most commonly used paper on machine QA and commissioning and the tests they describe are part of the Varian recommendations. However, as pointed out by the authors, the tests they devise do not thoroughly test the complete system and leave room for improvement.[48,49] Further, Ling *et al.* do not consider patient specific QA nor TPS QA. It is the aim of the present work to present a comprehensive commissioning and QA program for RA. This includes tests of the machine performance, the TPS and patient specific QA.

## II. METHODS AND MATERIALS

A comprehensive QA program was developed and tested in two radiotherapy departments to encompass the two most commonly used MLC types for RA delivery. Both departments use the full Varian (Varian Medical Systems Inc, Palo Alto, CA) solution for RA delivery: optimizations and forward dose calculations (AAA) are performed within the Eclipse planning system and delivered through the Aria record and verify system. Some additional calculations were performed with an Eclipse 10.0 beta version. The Herlev University Hospital (Herlev, Denmark) has eight 2300iX Clinacs (Varian) with 6 and 15 MV photon beam, all equipped with a 120 Millennium MLC while the Clinique Sainte Elisabeth (Namur, Belgium) also has a Novalis TX Clinac (6MV, 6MV SRS, and 18MV) with a 120 high definition MLC and RA capability. All are equipped with a Varian aS1000 amorphous silicon (aSi) portal imager (EPID) with dosimetric (integrated) acquisition mode.

The dosimetric equipment used during the RA implementation program is outlined in Table I. An Octavius phantom with a Seven29 2D ion chamber array (PTW, Freiburg, Germany) and VERISOFT analysis software is present in both centers, as is the PTW StarCheck ion chamber array and the included software. The Herlev hospital also has the Delta4 system. Both centers have established a Gafchromic EBT film (International Specialty Products, Wayne, NJ) dosimetry program. The films are scanned by means of an Epson Flatbed (Epson Perfection V700) and converted to dose by means of the VERISOFT FILMSCAN (version 2.7) software. The VERISOFT FILMSCAN software allows automatic selection of the red color component only, performs a flatness correction (based on the scan of a nonirradiated film) and a conversion from density to absolute dose through a user defined calibration curve. Film analysis is performed with the VERISOFT (4.1) software.

### II.A. Machine QA

Setting up a reliable and relevant machine QA protocol for RA delivery requires a clear understanding of the (presumed) interplay between the different players. A RA plan consists of a sequence of control points, each specifying the MLC position and gantry angle at a given cumulative MU output. In between subsequent control points, the MLC and gantry angle

TABLE I. Overview of the used measurement equipment for the different parts of the RA validation protocol. Letters indicate during which phases the setups are used: I = implementation, R = routine, P = problem investigation or U = major upgrade.

| | Machine QA | | | | TPS validation | | |
|---|---|---|---|---|---|---|---|
| | Static Twinkle | Dynamic Twinkle | Sunrise | Snooker Cue | AAA | PRO + AAA | Patient QA |
| Gafchromic film +Epson scanner (+VERISOFT FILMSCAN) | I,P | I,P | I,P | — | I,P[a] | I,U[a] | I,(R)[a] |
| StarCheck + BeamAdjust +inclinometer (+MATLAB) | I,P | I,P | I,P | — | — | — | — |
| Seven29 + Verisoft +inclinometer +MATLAB | I,P | I,P | I,P | — | — | — | — |
| +solid water | — | — | — | — | I,P | — | — |
| +Octavius phantom | — | — | — | — | — | I,U | I,R |
| Delta4 | — | — | — | — | — | I,U | I,R |
| EPID | — | — | — | I,U,R[b] | — | — | I,R[c] |

[a]Including at least one additional ion chamber point measurement for absolute dose verification.
[b]Including the placement of a metal rod, protruding from a block on the treatment couch.
[c]To be used in combination with at least one additional check such as an ion chamber point dose measurement or an independent point dose calculation.

move from the original to the newly specified position while the beam remains on and delivers the specified amount of MU, lowering the dose rate, gantry, or MLC speed as needed. For the current RA solution, the control mechanisms behind the actual delivery are as follows. The nominal dose rate is specified by the user and is typically set to the maximum possible value for treatment efficiency reasons (i.e., 600 MU/min in our case). In Eclipse, the maximum gantry speed is limited to 4.8 deg/s and the maximum MLC speed is user definable, but set to the recommended value of 2.5 cm/s. At the treatment console two separate sequences are generated to control the Clinac behavior; one specifying the MLC positions versus gantry angle, the other specifying the MUs versus gantry angle. Before the actual delivery, the plan is checked for possible violations to predefined limits. The limits set at the machine are less stringent than in Eclipse to allow for some margin. The gantry speed has a range of 0.5–6 deg/s. Except for doseless segments, the MUs/deg are required to be larger than 0.2 but smaller than 20 (60 for the 6MV SRS mode). During delivery, control is taken by the slowest player: when less than ~1.7 MU/deg are to be delivered, the gantry will move at maximum speed but the dose rate will drop below 600 MU/min.[50] When more MU/degree are to be delivered, the maximum dose rate will be maintained and the gantry will slow down. If the MLC can not perform its movement adequately fast, it will not induce a drop in the dose rate (and/or a slowing down of the gantry) like it does in a dynamic IMRT delivery, but it will generate an interlock instead.[51]

A selection of tests has already been proposed by Ling *et al*.[6] As stated by the authors, these tests assess the correct behavior of the MLC as a function of MU, but do not include any verification of the angular accuracy as the film (or EPID) is mounted to the gantry. In addition, we have therefore developed a number of tests that focus on the gantry performance in relation to the MUs and MLC position, respectively. The dose rate, gantry speed and MLC trajectory of these tests is shown in Fig. 1:

#### II.A.1. Static MLC Twinkle: assessing the accuracy of dose rate modulation versus gantry angle (maximum acceleration and deceleration).

The "Static Twinkle" [Fig. 1(a)] is an artificially programmed RA delivery during which the MLC leaf positions remain in a stationary position, forming a 1 mm wide central gap. Dose is only delivered from a limited amount of narrow angular sectors (2° each), separated by larger (38° each) doseless sectors. During the doseless segments, the gantry moves at maximum speed. For the narrow sectors of dose delivery, the MUs and nominal dose rate are selected such that they require minimal gantry speed and therefore maximum deceleration or acceleration in between, straining the machine performance to the allowed limit. By decreasing the total amount of MUs, the same plan can also entirely be delivered at constant gantry speed eliminating the effects of acceleration and/or deceleration for comparison. To simulate possible problems, artificial errors were introduced into the RA delivery. A too slow response in the gantry movement is simulated by shifting the dose rays over 1°, 2°, and 3°, respectively. An overly smoothened gantry steering is simulated by broadening the rays by 1°, 2°, and 3°, respectively.

#### II.A.2. Dynamic MLC Twinkle: assessing the accuracy of MLC movement versus gantry angle (maximum MLC speed)

The Dynamic MLC Twinkle [Fig. 1(b)] should result in a measurement that is identical to the Static Twinkle, but the MLC positions no longer remain static during the doseless angular sectors; they perform a sweeping motion at maximum leaf speed. They are programmed to have returned to the

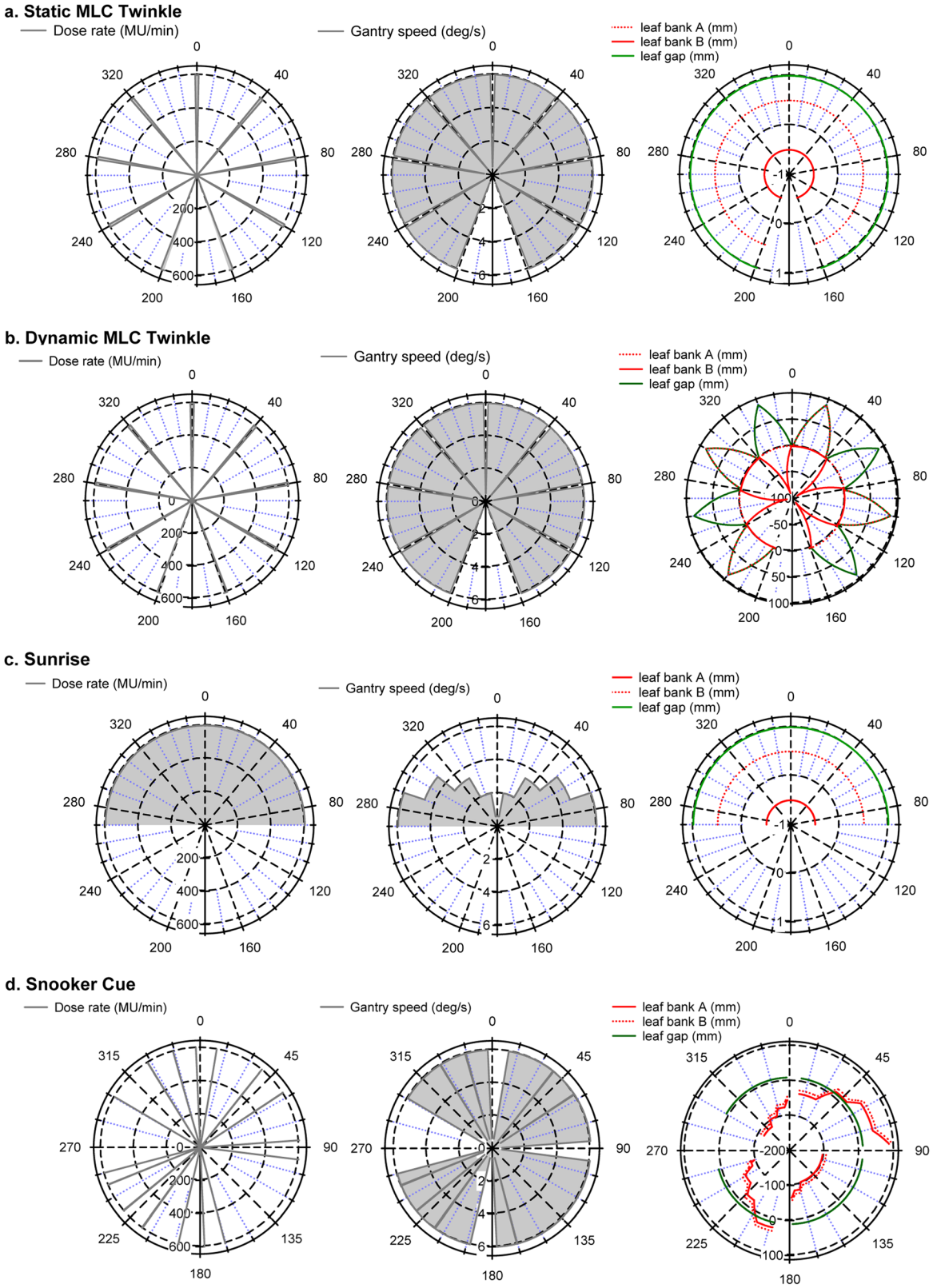


FIG. 1. Polar graphs displaying the programmed dose rate, gantry speed and MLC leaf positions as a function of gantry angle for (a) the Static MLC Twinkle, (b) the Dynamic MLC Twinkle, (c) the Sunrise and (d) the Snooker Cue for machine QA.

central gap position at the start of the narrow dose ray delivery and should not move away from this position until the dose delivery over this angular sector has completed. Imperfections in the synchronization between leaf position and gantry movement will result in narrowing, broadening or angular displacement of the rays. Such errors are again simulated by programming 0.2, 0.5, and 1 mm errors in the MLC positions of the artificial files.

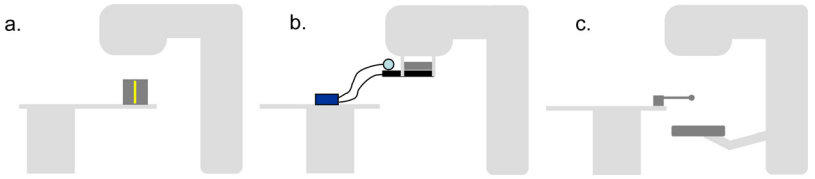


FIG. 2. Experimental setups for the machine QA tests: (a) Gafchromic film in transversal plane through the isocenter in $10 \times 10$ cm$^2$ solid water blocks, (b) 2D ion chamber array with inclinometer mounted to the tray holder of the Clinac and (c) EPID with metal rod placed on the treatment couch.

#### *II.A.3. Sunrise: assessing the impact of gantry speed, gravity and inertia on the gantry angle precision*

The Sunrise delivery [Fig. 1(c)] consists of adjacent dose sectors (of 20° each) of increasing total dose levels when moving from gantry 270 to gantry 0, subsequently decreasing again when moving from gantry 0 to gantry 90. The arc is programmed to be perfectly symmetrical around gantry 0. Dose is delivered through a narrow (1 mm) static MLC opening with constant gantry speed within each angular sector but subsequent sectors require a different amount of MUs per sector. The MUs are chosen sufficiently high to enforce maximum dose rate throughout the whole delivery and to impose minimum gantry speed in the highest dose sectors and maximum speed in the lowest dose sectors. Whereas gravity is opposing the gantry's inertia during the upward gantry motion (270–0), it adds to the inertia in the downward trajectory (0–90). The transition from one sector to the next is a sharp one and—if present—gravitational effects on the delivery are expected to show up at the borderlines, causing an asymmetry in the delivered dose. Here again, artificial errors were introduced to simulate such effects.

#### *II.A.4. Snooker Cue: combining MU versus gantry angle and MLC movement in one single test*

A final test [Fig. 1(d)] was designed to allow a quick routine assessment of the correct interplay between gantry angle, MLC position, and dose delivery in one single treatment plan by means of the EPID. Mounted to the gantry, the EPID has the major advantage that it allows extremely fast and easy measurement setup and data acquisition. As a disadvantage, it rotates along with the gantry so without additional input, the integrated image does not include gantry angle information. For the Snooker Cue test, a simple setup was attached to the end of the treatment couch consisting of a thin metal rod with a spherical tip (diameter = 5 mm) mounted in the longitudinal direction with a lateral and vertical displacement from the isocenter of 5 cm and 10 cm, respectively. The MLC was programmed to have a constant gap of 1 cm between opposing leaves at all times. The position of the gap was programmed such that for a selection of gantry angles, the metal rod should be precisely in the centre of the projection of the MLC gap, while making sure that subsequent projections of the gap (at source imager distance 150 cm) remain clearly separated. Dose delivery was programmed solely for narrow angular sectors (0.4 deg) around these discrete gantry angles, again assuring maximal gantry acceleration and deceleration between doseless and maximal dose rate delivery. In addition, the displacement of the MLC gap from one position to another was delayed as long as necessary to enforce maximum leaf speed before coming to an abrupt halt at the moment of dose delivery. The treatment plan is subdivided into four subarcs with one integrated image each, to allow a clear distinction between the gap projections of the different quadrants. The treatment plan was programmed in clockwise as well as in counter clockwise direction.

The tests were performed using different measurement methods (Table I and Fig. 2):

*II.A.4.a. Gafchromic film.* For the Twinkle and Sunrise tests, first, gafchromic film was cut into $10 \times 10$ cm$^2$ pieces. For each test, one such piece was placed between two custom cut ($10 \times 10 \times 5$ cm$^3$) solid water blocks and positioned on the treatment couch in the transversal plane through the isocenter. The isocenter (and the gantry zero position) is marked on the film with four black dots. The film is then irradiated with the test field and inspected visually on the spot, but left to fully auto develop overnight before being scanned. The films are scanned and converted to dose by means of the VERISOFT software, automatically extracting the red component from the film. A scan of a large nonirradiated film is used as a background and flatness correction.

*II.A.4.b. 2D ion chamber array with additional inclinometer.* A second, alternative setup was developed for the Twinkle and Sunrise tests, aiming to avoid the use of film in clinical routine. A special fixation plate was made to mount the StarCheck or Seven29 ion chamber array together with an inclinometer (FAS-A, MicroStrain, Williston) to the tray holder of the Clinac. The inclinometer signal (gantry angle) and the array data (integrated dose) are read out simultaneously every 100 ms (StarCheck) or 200 ms (Seven29). A dedicated software interface was written in MATLAB (MathWorks, MA) to allow data processing and visualization of the acquired data as a function of gantry angle.

*II.A.4.c. EPID:* The "Snooker Cue" RA fields were imported into Eclipse, scheduled and measured through Aria with the EPID at a source axis distance of 150 cm and using the integrated image acquisition mode. The images can be visually evaluated on-line or in the offline review software but need to be evaluated in the Eclipse Portal Dosimetry workspace if absolute dose information is to be obtained as well.

### II.B. TPS validation

#### *II.B.1. AAA validation for manually programmed RA-specific fields*

In the Eclipse environment, the total dose of a RA plan delivery is calculated by means of the AAA algorithm[52,53] as

the sum of a large number of static gantry, dynamic MLC fields. The default calculation settings are such that every control point is represented by one such static field. Even though the dose calculation makes use of a previously known and validated algorithm,[53,54] the conditions under which it is now used are usually not covered by the standard validation tests, neither for static nor for dynamic MLC treatments. The dose calculation algorithm fundamentally differs from static MLC calculations as it makes use of an interpolated photon fluence, taking the linear MLC movement in between control points into account. This is an approach similar to the IMRT dose calculation. However, the changing angular incidence in between control points is ignored and the fluence is assumed to originate from the gantry angle specified by the control point. Obviously, the angular resolution of the control points needs to be sufficiently high for this approximation to be valid. Should the user wish to do so, the angular calculation resolution can be changed from the default control point based resolution to a fixed angular resolution (1°–5°). In addition, one needs to bear in mind that the typical MLC shapes appearing in a RA delivery are usually not represented within the standard validation package of a dose calculation algorithm (e.g. AAPM guidelines). Some of the segments have very small and/or off-axis effective openings in relatively large collimator openings, representing a challenge for the accurate absolute dose calculation. In addition, leaf pairs with nearly closed MLC tips (0.6 mm opening) within the field are commonly observed. The importance of the resolution of the calculation grid is therefore another item to be investigated. As leaf movement can sometimes be highly asynchronous, it is expected to give rise to considerable tongue and groove effects, only modeled in the recent versions of the fluence calculator (Leaf Motion Calculator version 8.6 and later).

To assess the impact of these RA-specific parameters (MLC parameters, small, off-axis MLC fields in large collimator opening, angular, and calculation grid resolution), we have first performed a number of tests on individual static fields followed by a set of artificially programmed arc deliveries. The values used for the dosimetric leaf gap (DLG)—modeling the rounded leaf tips—and leaf transmission are the ones determined during the implementation of IMRT by means of the Dynamic Chair[55] and the Sweeping Gap[56] tests. The tongue- and groove parameters are predefined for each type of MLC and can not be modified by the user. For all tests, calculations were performed with the calculation grid set to 2.5 and 1 mm. Except where indicated otherwise, the default control point angular resolution was used for the arc calculations. Tests were performed for both MLC types and for all available photon energies.

The tests visualized in Fig. 3 were mostly performed in a rectangular phantom, (consisting of $30 \times 30$ cm$^2$ solid water plates), at a depth of 5 cm and SSD = 95 cm (for gantry = 0°). Only the machine QA tests that were also used for the validation (Static MLC Twinkle and Sunrise) were performed in the setup described in the previous paragraph. Measurements were performed with Gafchromic films, but the absolute dose level of the film was always double checked by means of measurements with the StarCheck, the Seven29 or a single ion chamber (PTW 0.125 cc Semiflex). The drawings in Fig. 3 correspond to the Millennium120 MLC setup. They would be very similar for the HD MLC, apart from the amount of leaves involved in the $4 \times 4$ cm$^2$ central opening and the position of the jaws relative to the leaves.

The first tests [Fig. 3(a)] aim to simultaneously address the modeling of the rounded leaf tips (DLG) and the small, off-axis MLC openings in relatively large collimator settings. The field size was chosen such that the measurement includes information on both leaf widths for both MLCs (i.e., 5 mm and 1 cm leaves for the 120Millennium MLC, 2.5 and 5 mm leaves for the HD MLC) while not exceeding a total size of 24 cm to remain within the maximum dimensions of the film or the 2D array. For the setup displayed in Fig. 1(a), four MLC files were created in which the central leaves always form a $4 \times 4$ cm$^2$ open square, while all the other leaves line up to form a very narrow gap of 1, 3, and 5 mm, respectively. The second test setup is very similar to the first, except that all the leaf positions were shifted 10 cm off-axis.

Additionally, the absolute dose in the centre of the $4 \times 4$ cm$^2$ openings was measured for an extended range of main collimator settings—varying from a $4 \times 4$ to a $24 \times 40$ cm$^2$—to assess the accuracy of the MU calculation.

Second, Fig. 3(b) shows the test used to assess the modeling of the tongue and groove effect in a worst case scenario: two static fields were delivered with complementary patterns of extended and retracted leaves. Again, the central leaves were kept in an open position in both fields to permit a reliable absolute ion chamber point dose measurement. Like in the first test, the collimator settings were chosen to include both leaf widths.

In Figs. 3(c)–3(e), the aspects of the above tests are combined into an arc delivery and calculation. These tests were performed for a limited arc section to obtain higher measurement precision (i.e., with no significant angular dependence of the measurement equipment) and allow high resolution calculations while keeping calculation times reasonable. The MLC files were programmed to mimic both simple [Fig. 3(d)] and extreme [Fig. 3(e)] movements that will be generated by the RA optimizer: RA treatment planning aims for maximum gantry speed at all times and therefore will not allow MLC movements beyond 0.52 cm/deg (i.e., 2.5 cm/4.8°). Every MLC pair was programmed to perform a 2 cm sweeping gap motion at maximum speed over a total trajectory of 8 cm per leaf, while the gantry is also rotating at maximum speed, moving from 345° to 15°. At 600 MU/min this requires a 63 MU delivery. Increasing the MU will cause the gantry rotation to slow down, decreasing the MUs below 63 is likely to cause an MLC interlock during delivery. In setup d, the leaves perform a perfectly synchronous movement, all moving simultaneously from left to right and back. In setup e, adjacent leaves move in opposing directions, sweeping either from left to right (and back) or from right to left (and back), thereby introducing the dosimetric consequences of the tongue and groove shapes in the MLC leafs. Again, field sizes were chosen to include both leaf types into

| | Gantry and MLC | Collimator settings (cm) | |
|---|---|---|---|
| | | Millenium120 MLC | HD MLC |
| a. | static gantry, DLG and OF<br>G = 0<br> 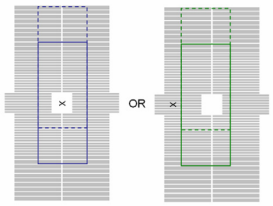 <br> | DLG<br>*central :*<br>X=14,Y=24 (—)<br>X=14,Y1=4,Y2=20 (---)<br>*off-axis :*<br>X1=-2,X2=16,Y=24 (—)<br>X1=-2,X2=16,Y1=4,Y2=20 (---) | DLG<br>*central :*<br>X=14,Y=20<br><br>*off-axis :*<br>X1=-2,X2=16,Y=20 |
| | | OF<br>*central :*<br>X=4…24, Y=4…40<br>*off-axis :*<br>X1=-2,X2=16,Y1=4,Y2=4…20 | OF<br>*central :*<br>X=4…24, Y=4…40<br>*off-axis :*<br>X1=-2,X2=16,Y=4…20 |
| b. | static gantry, TnG<br>G = 0<br> 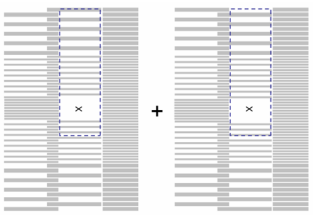 <br> | *central :*<br>X=14,Y1=4,Y2=20 (---) | *central :*<br>X=14,Y=20 |
| c. | dynamic Gantry, static MLC<br>- G = 345 → 15<br> 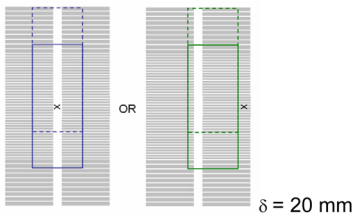 <br><br>- Static Twinkle G = 200 → 160<br>- Sunrise G = 200 → 160 | *central :*<br>X=14,Y=24 (—)<br>X=14,Y1=4,Y2=20 (---)<br><br>*off-axis :*<br>X1=-2,X2=16,Y=24 (—)<br>X1=-2,X2=16,Y1=4,Y2=20 (---) | *central :*<br>X=14,Y=20<br><br>*off-axis :*<br>X1=-2,X2=16,Y=20 |
| d. | dynamic Gantry, dynamic MLC: sweeping gap<br>G = 345 → 15<br> 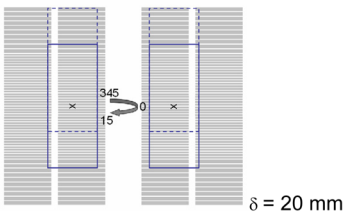 <br> | *central :*<br>X=14,Y=24 (—)<br>X=14,Y1=4,Y2=20 (---) | *central :*<br>X=14,Y=20 |
| e. | dynamic Gantry, dynamic MLC: TnG<br>G = 345 → 15<br> 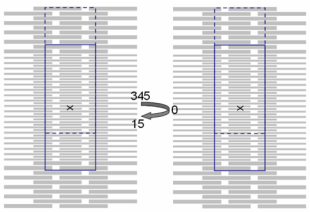 <br> | *central :*<br>X=14,Y=24 (—)<br>X=14,Y1=4,Y2=20 (---) | *central :*<br>X=14,Y=20 |

FIG. 3. Schematic overview of the MLC shapes and the field sizes used for the basic validation of the dose calculation. The drawings correspond to the Millenium120 MLC setup, but are very similar for the HD MLC. The cross marks the CAX and the $\delta$ indicates the leaf gap(s) between opposing leaf tips. The collimator settings are indicated first for the central setup and second for the laterally or longitudinally shifted setup. All measurements were performed at a depth of 5 cm and SSD = 95 cm, except the Static Twinkle and Sunrise test which were performed in the setup shown in Fig. 2.

the measurement. For the actual delivery, two control points suffice to describe the entire movement as the MLC controller automatically performs an interpolation to generate its own 50 ms check points during the delivery. Even so, a series of MLC files were created, all corresponding to what should be the same delivery, but with varying degrees of angular resolution in the control points, ranging from control points every 15° (i.e., most simplistic, original treatment delivery file) to every 3° and 1.5°. For all resolution levels, measurements were performed and the corresponding dose was calculated with the default control point based angular resolution. In addition, the calculations were rerun with the angular resolution level modified to a fixed value of 1°.

### *II.B.2. Performance assessment of the RA optimization algorithm*

The RA plan optimization in the Eclipse environment is performed by the progressive resolution optimizer (PRO8.9) algorithm. After having defined the isocenter, the dose prescription and the angular range of the arc(s) to be used, the user launches the optimization. It has a similar interface as the IMRT optimizer, allowing the user to specify upper, lower or line constraints on the target volumes and organs at risk (OAR), each with its own priority. A user definable normal tissue objective applies a penalty to the normal tissue dose as a function of the distance to the target volume aiming to reduce hot spots outside the target volume(s). An additional constraint (minimum and maximum) can be applied to the total amount of MU and avoidance sectors can be defined. Before starting the actual optimization process, the user has the possibility to launch the automatic optimization of the collimator angle, the isocenter position and the couch rotation. The main collimator opening as determined at the start of the PRO optimization process remains fixed during the whole arc delivery.

In contrast to the Eclipse IMRT process, the PRO is not an optimal fluence based but a direct aperture optimizer.[10] Optimization of the leaf positions is performed during five subsequent "resolution levels". Each level is characterized by a predefined increase in angular resolution. For a 360° arc, at the first resolution level (i.e., at the start of the optimization) about 10 equi-angular fields are used. The initial positions of the leaves are set to conform around the target volume. The MLC aperture is then optimized according to the constraints, but always such that the leaf motions do not violate the maximum allowed leaf speed. At the second resolution level, the amount of fields is doubled and the MLC aperture is optimized further. At the third, fourth and fifth level, the amount of fields is again increased and the field aperture optimized, resulting in a final angular resolution of around 2°. The user can interactively change the constraints and priorities during the course of all levels, but the response of the algorithm to such changes is at its most efficient during the first resolution level.

Evaluating the performance of a new algorithm by means of real patients is a difficult and often inadvertently subjective task. Because of the patient specific volumes, plan comparisons are often difficult to interpret in terms of target coverage and target conformity versus organ sparing. In addition, the results depend substantially on the experience and time spent by the planner on one technique or the other. In order to limit these intrinsic problems in algorithm evaluations, we present a set of simple geometric structures, meant to mimic simplified clinical cases. Some of the structures are similar to the ones proposed in the AAPM TG-119 IMRT commissioning test instructions while others have been added to provide a more extensive training and validation set for arc treatments. Except for the "'Lung," all structure sets were contoured on a scan of the homogeneous Octavius phantom with solid water inserts in the cavity for the Seven29. A selection of the used geometric structure sets is illustrated in Fig. 4.

- Central and off-axis cylinder [Fig. 4(a)]: Two simple cylinders—one central (diameter 10 cm) and one off-axis cylinder (diameter 5 cm) at a 5 cm off-axis position—are used to investigate central versus off-center RA treatments. For RA treatments, the isocenter must often remain in the center of the patient even if the target is not, as lateral movement of the treatment couch must be limited to avoid collisions during the arc movement of the gantry.
- Spherical prostate [Fig. 4(b)]: this structure set consists of a spherical prostate and a cylindrical rectum and bladder.
- Cylindrical prostate with seminal vesicles (not shown): this structure set consists of three cylindrical structures (prostate, rectum, bladder) and two half-moon structures alongside the "prostate" cylinder to represent the seminal

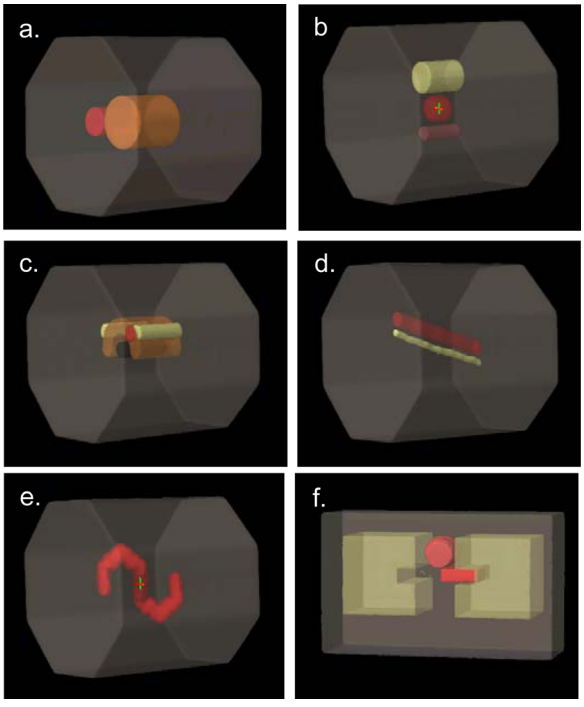


FIG. 4. Some illustrations of the artificial structures contoured in the Octavius: (a) central and off-axis cylinder, (b) spherical prostate with bladder and rectum, (c) horseshoe-shaped head and neck volume with two PTVs, (d) oesophagus and spinal cord tilted cylinders, (e) spiral shaped Snake structure. Heterogeneity tests were performed in the home made inhomogeneous lung phantom displayed in (f).

vesicles and generate a more concave total target, around an organ at risk. This structure set can also be used to simulate integrated boost treatments with different simultaneous dose/fraction prescriptions to different volumes.
- Head and Neck (with one or two PTV structures) [Fig. 4(c)]: A horseshoe-shaped large PTV and a slightly off-axis cylindrical volume simulate a simplified head and neck situation, including a cylindrical structure as the spinal cord or brainstem and two half-moon cylinders alongside the larger PTV to represent the parotid glands.
- Oesophagus [Fig. 4(d)]: A tilted cylindrical volume simulates an elongated target volume with increasing depth in the longitudinal direction. A "spinal cord" cylinder runs parallel along the target.
- Snake [Fig. 4(e)]: The "snake" is a highly complex, spiral shaped tube designed to challenge both the optimization and the delivery.
- Lung [Fig. 4(f)]: A lung phantom was constructed out of $30 \times 30$ cm$^2$ solid water plates and $5 \times 10$ cm$^2$ custom cut solid water and cork building blocks of variable thicknesses (ranging from 2 mm to 5 cm). A solid water "mediastinum" with protruding lobes was thus constructed in between two cork lung structures. A first rectangular target volume was contoured including the right lobe and extending to the middle of the mediastinum. A second, cylindrical target volume was contoured in the upper part of the central pillar of the mediastinum.

For all of the above structure sets, a series of RA plans were optimized, exploring the different options that can be employed during optimization (e.g., collimator rotation, isocenter optimization, …). Plans were generated in both centers for the Millennium120 and in Namur for the HD MLC. When optimizing different plans on the same structures but with changing initial conditions (e.g., user defined versus automatically optimized collimator rotation), the exact same criteria (constraints and priorities) were used to allow systematic inter comparison of the different plans. To evaluate target coverage, we make use of the mean, maximum and minimum doses. We also calculate the conformity index for the 95% isodose level ($CI_{95}$) as a quick initial assessment in combination with visual isodose evaluation:

$$CI_{95} = V_{95}/V_{PTV}.$$

As the conformity index itself only assesses the size of the 95% volume but not its anatomical location with respect to the target volume it should be used with caution and never as a sole decisive factor.[57,58] To allow more detailed quantitative assessment we have made use of two additional criteria, the lesion coverage fraction (LCF, also referred to as the lesion CoVerage factor CVF) and the normal tissue overdosage fraction (NTOF).[58] The LCF measures the fraction of the PTV that is covered by the desired isodose level (e.g., 95%). If the PTV was not entirely within the 95% isodose, we used the Boolean operators available in the Eclipse contouring workspace to create a "PTVand95" structure, composed of all pixels that belong to both the PTV and to the structure generated from the 95% isodose. The LCF is then calculated by taking the ratio of the volume of the PTVand95 structure to the PTV volume:

$$LCF_{95} = V_{PTVand95}/V_{PTV}.$$

If the PTV is entirely within the 95% isodose, obviously, $V_{PTVand95}$ equals $V_{PTV}$ and $LCF_{95}$ therefore equals unity. In addition to the LCF value, a measure for the relative amount of high dose delivered outside of the PTV is obtained by subtracting all PTV pixels from the 95% dose volume to obtain a "95subPTV" structure. The ratio of the volume of this structure to the volume of the 95 isodose structure yields the $NTOF_{95}$:

$$NTOF_{95} = V_{95subPTV}/V_{95}.$$

The NTOF is very similar to the healthy tissue overdosage factor (HTOF) parameter described in Ref. 58, except that we have chosen to normalize to the $V_{95}$ instead of to the PTV volume, in order to quantify the percentage of the 95% dose volume that is delivering "useless" dose to normal tissue. In plans of good quality, were the 95% isodose line closely encircles the PTV, both parameters yield approximately the same values.

The ideal target coverage would be characterized by a $CI_{95}$ and $LCF_{95}$ close to unity and $NTOF_{95}$ approaching zero. Inter comparison of the above values for different plans on the same target volumes allows quantitative interpretation of the relative plan quality.

#### *II.B.3. AAA validation of RA plans on artificial structures*

For all of the above generated plans, measurements were performed in a phantom and compared to the corresponding dose calculation. Three different verification methods were used in parallel:

- Gafchromic film in the homogeneous Octavius phantom ("red face") or in the Lung phantom
- Seven29 in the Octavius phantom ("black face")
- Delta4 (ScandiDos, Uppsala, Sweden)

The use of Gafchromic films is an established method for general phantom QA,[59] as is the Seven29-Octavius combination for arc measurements.[60] The reliable absolute dose level but limited resolution of the Seven29 measurement is complemented by the more cumbersome, but high resolution film measurement. Horizontal (coronal) and vertical (sagittal) planes were measured with the first two methods. The additional use of the Delta4 QA solution allows dose acquisition in two diagonal planes and provides an additional dataset for every plan. (Although the Octavius phantom also allows easy acquisition of diagonal planes, the corresponding calculated planes can currently not be exported from Eclipse nor can they be reconstructed in the current version of the VERISOFT software from the 3D dose export. Therefore, the diagonal planes were not acquired for the Octavius set up.) The goal of using three different measurement methods is to more extensively test the accuracy of the dose delivery

and calculation, while simultaneously testing out and inter comparing the different QA solutions for later use in clinical routine.

For the film verification, no dose recalculation on a phantom needed to be done as the film was irradiated in the same setup as was used for the optimization and forward calculation. Film processing and analysis was performed as described at the onset of the materials and methods section.

For the comparison with the calculated dose in the measurement plane, we exported both the 2D dose plane and the 3D dose matrix, to allow gamma analysis in two and three dimensions.[61,62] For the second and third phantom verification method, the original plan was transferred to the appropriate phantom (Octavius CT scan with the Seven29 and Delta4 cylindrical phantom, respectively) and the dose was recalculated. The presence of the treatment couch was always taken into account.[63]

### II.C. Patient QA

Although less important during the validation of a new technique, the efficiency of the QA process becomes a critical factor for the success with which the new technique can be transferred into clinical routine. We have focused on the two most common methods that are currently available (or in a final testing phase) to the medical physicist: phantom QA and portal dosimetry. For a cohort of ten patients with varying treatment sites, we have performed both patient specific QA methods and compared the results for consistency. We introduced some errors such as suboptimal MLC parameters and lack of couch modeling to test the respective sensitivity to error detection. We have monitored the time needed for each of the methods, distinguishing between preparation and analysis time and the time spent at the treatment machine.

#### *II.C.1. Phantom QA*

For RA patient QA in a phantom, we have used the exact same methods as described above for the general validation of the RA process, namely the Octavius/Seven29 combination (in the horizontal and vertical measurement plane setup), the Delta4 system and film. Although a new plan was created to calculate and export the expected dose in the phantom, at the treatment console, we did not deliver this copy but made use of the newly available (8.9) "QA mode" to deliver the actual patient plan to the phantom. The QA mode does not register the delivered session and therefore allows (repetitive) verification of the treatment plan without interfering with the recorded patient dose.

#### *II.C.2. Portal dosimetry*

Portal dose images were acquired with the aS1000 EPID using the dosimetric acquisition mode, integrating the delivery during the whole arc motion. The dosimetric calibration of the imager panel was performed at a source imager distance of 100 cm and included a two dimensional profile correction[64,65] instead of the official profile correction based on a diagonal $40 \times 40$ cm$^2$ field profile measurement at $d_{max}$. The source imaging distance was 100 cm to maximize the range of field sizes that fit into the $40 \times 30$ cm$^2$ imaging panel. The radiation was delivered directly to the panel, without the treatment couch or any kind of phantom in the beam. Although the positional accuracy of the exact arm is known to be far superior to the older R-arm, it is still known to exhibit some sagging ($\sim$1 mm) when rotated. To assess the impact of the sagging of the exact arm on the final image, a number of RA plans were converted into IMRT plans with the exact same MLC movement as a function of MU but with gantry zero.

The expected portal dose images were calculated by means of the portal dose prediction algorithm available in the Eclipse 10.0 beta version. This is fundamentally the same algorithm as used for the IMRT portal dose verification,[64] converting the total theoretical fluence into a portal dose image while taking the scatter characteristics of the aSi into account through a single pencil beam algorithm. As the EPID rotates along with the gantry, the gantry angle information in the treatment plan is not used during the prediction and the whole delivery is collapsed into the plane of the imager panel.

Portal dose images were measured and calculated for all RA treatment plans produced on the artificial structures in Octavius and for all patient plans. The results were compared in the Portal Dosimetry software packaged of the 10.0 Eclipse environment, mainly based on visual line profile comparison and 2D gamma calculation [using Gamma criteria of 3% (global dose), 3 mm and requesting at least 95% agreement when restricting the region of interest to the MLC CIAO].

## III. RESULTS

From the results obtained from the diverse test set-ups, we have made an assessment of their general applicability in combination with the used equipment. Table I illustrates during which phase they are deemed to be most useful, i.e., during RA implementation (I), in routine (R) for problem investigation (P) or after a major upgrade (U).

Detailed results on the different phases are presented below.

### III.A. Machine QA

Results on the static MLC twinkle tests are illustrated in Fig. 5. The polar graphs of Fig. 5(a) show the theoretically programmed dose rate behavior as a function of gantry angle as solid gray bars. The lines represent the measurements, obtained from the simultaneous data acquisition with the inclinometer and the StarCheck 2D array. Correct delivery is illustrated in the upper graph. Only data for the central chamber are shown, but the results for the other chambers along the longitudinal axis of the StarCheck are very similar to the ones displayed. The expected Twinkle pattern is accurately reproduced by the measurement. The errors shown in the bottom part of Fig. 5(a) correspond to an artificially introduced gantry inertia effect of 3° (red line) and a 2° smoothening effect of the gantry motion around the actual control point (green line). The inertia error shows up as a

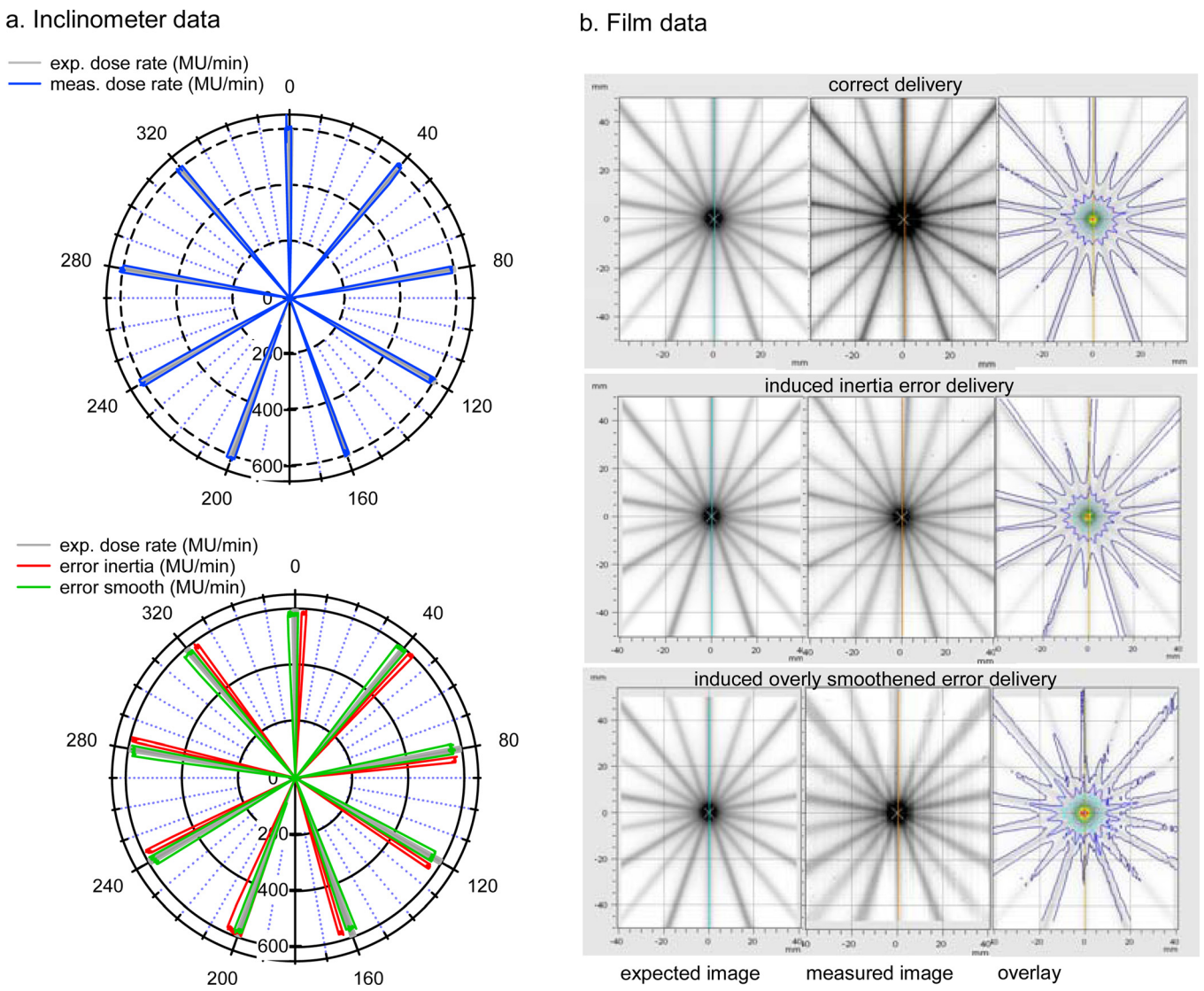


FIG. 5. Examples of machine QA measurements: (a) StarCheck and inclinometer data obtained for the Static MLC Twinkle data for correct delivery (upper polar plot) and delivery with intended errors (lower polar plot). The gray bars indicate the theoretically expected dose rate as a function of gantry angle. The errors shown in the lower part correspond to an artificially induced gantry inertia effect of 3° and a 2° smoothening effect of the gantry angle motion. (b) Film data obtained for the Static MLC Twinkle displaying correct delivery, induced inertia effect and overly smoothened delivery. All comparisons show the expected image, the measured film and the isodoses of the measurement overlayed on the expected image.

clockwise shift of the angles at which the dose rate peaks are observed (except for the starting point, which correlates correctly as no inertia is present at the onset of the arc rotation). The smoothening error shows up as a widening of the observed dose rate peaks. Artificially introduced errors smaller than 1° (not shown) do not distort the measurement enough to be clearly visible. A similar sensitivity to error detection is observed when using films [Fig. 5(b)] instead of the StarCheck/inclinometer combination. Next to the expected and measured images, an overlay of both is displayed: the isodose lines indicating the measured rays coincide well with the expected rays (shown in grayscale) during correct delivery, but show a displacement or widening for the rays with artificially introduced errors. Errors of 1° or less are barely distinguishable. Results for the dynamic MLC Twinkle are very similar to the ones shown for the static MLC twinkle. After correct delivery, the obtained data are identical to the static MLC Twinkle data. Artificially introduced errors in the MLC movement show up as a displacement, narrowing or widening of the dose rate peaks, resulting in polar graphs and images similar to the ones shown in Fig. 5.

The Sunrise data obtained with the StarCheck/inclinometer tandem are evaluated by means of polar graphs displaying the measured dose (instead of the above used dose rate) as a function of gantry angle. Measurements showed an adequately sharp transition in gantry speed in between subsequent sectors and a stable gantry speed within the sectors. As theoretically intended, the dose rate remains at its maximum value of 600 MU/min during the whole delivery. (The planar dose distribution as measured by the film in the transversal plane is not shown here but elaborated on in Fig. 8(a), where it is also used for the validation of the dose calculation algorithm).

The integrated image of one of the subarcs (gantry 270–0°) of the Snooker Cue test is shown in Fig. 6(a). As can be seen, the metal rod remains in the center of the projected MLC gaps for all gantry angles. In contrast to the Twinkle and Sunrise measurements, programmed errors of 1° in the gantry position were already quite noticeable as the projection of the probe shifts notably out of its central position in the projection of the MLC gaps (Fig. 6(b)]. For gantry angle errors of 2° [Fig. 6(c)] or more, the probe's projection drifts out of the MLC projection. A similar effect was observed for the plans containing a 1 and 2 mm intentional MLC error, simulating the hypothetical situation in which the MLC has not reached its target position in time or with insufficient accuracy.

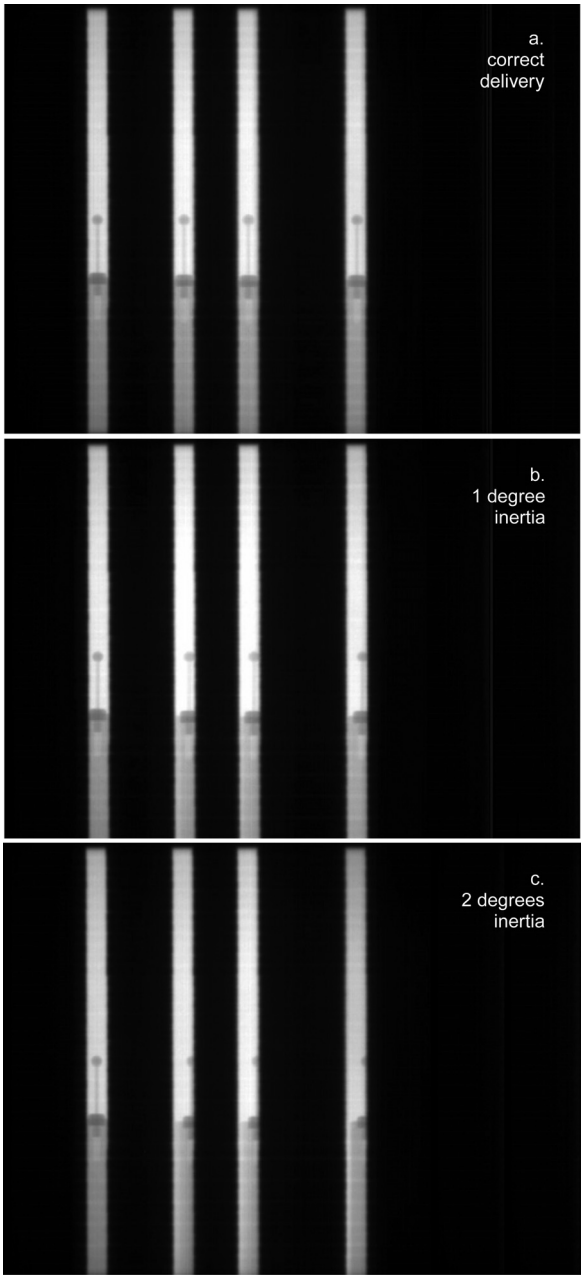


FIG. 6. Integrated images of one of the subarcs of the Snooker Cue test: displaying the rod in the center of the projected MLC gaps for all gantry angles for the correct delivery (a) and the displaced projection of the metal rod in the vertical lines for the simulated inertia error of 1° (b) and 2° (c) (for all gantry angles except the starting angle).

## III.B. TPS validation

### *III.B.1. AAA validation for manually programmed RA-specific fields*

For the static gantry MLC tests [Figs. 3(a) and 3(b)], we observe that the ion chamber measurements in the centre of the $4 \times 4$ cm$^2$ MLC openings agree within 2% with the calculated absolute dose for all collimator settings, for the central as well as for the off-axis MLC position. To evaluate the accuracy with which the different leaf gaps between opposing leaves are calculated, film data, and calculated dose planes are carefully aligned before extracting line profiles perpendicular to the leaves and precisely through the center of the leaf gap. Examples of such line profiles are shown in Fig. 7 for a 3 mm wide leaf gap for both MLC positions {central [Fig. 7(a)] and off-axis [Fig. 7(b)]} of the HD MLC. Although these data confirm the excellent absolute agreement in the $4 \times 4$ cm$^2$ opening, they also demonstrate the fact that the height of the dose peak between the leaf tips is underestimated by the 8.9 AAA dose calculation. The agreement is much better for the data obtained for the 5 mm gap, but worse for the 1 mm leaf gap. Enhancing the calculation resolution from 2.5 to 1 mm results yields only a marginal improvement, as this resolution change only affects the AAA forward calculation but not the default 2.5 mm resolution of the fluence that is used as input for the AAA dose calculation. When recalculating the dose distribution with the 10.0 beta version of the AAA algorithm, using a high resolution (0.3 mm) fluence calculation, near-perfect agreement with the measured data is observed for the 1 mm forward dose calculation resolution. The consequences of the improved resolution in the fluence calculation are also clearly visible in the tongue and groove test [Fig. 7(c)]: although the AAA 8.9 dose calculation reports an adequate average dose level, AAA 10.0 actually reproduces the pattern of dips and peaks, even for the 2.5 mm narrow central leaves of the HD MLC.

The dynamic gantry, static MLC tests provide clear feedback on the impact of angular resolution. When performing a dose calculation purely based on the manually programmed control points, the calculated dose can differ substantially from the measured dose. Figure 8(a) illustrates the drastic effect of the 15° angular resolution of the Sunrise test on the dose calculation: instead of spreading the dose (delivered through the 1 mm static MLC opening) over the entire angular sectors, the dose calculation assumes the full dose to be delivered solely at the control points, resulting in an unrealistic star-like dose pattern. When changing to a fixed angular resolution of 3°, calculation results approach reality, although the star-like pattern is still visible as can be seen from the oscillations in the line profile. A fixed angular resolution of 1° adequately reproduces the smooth dose delivery observed on film. A similar effect can be observed from the dynamic gantry sweeping gap test [Fig. 8(b)]: although an angular resolution of 15° suffices to produce the desired Clinac behavior, it results in an erroneous dose calculation. Again, setting the

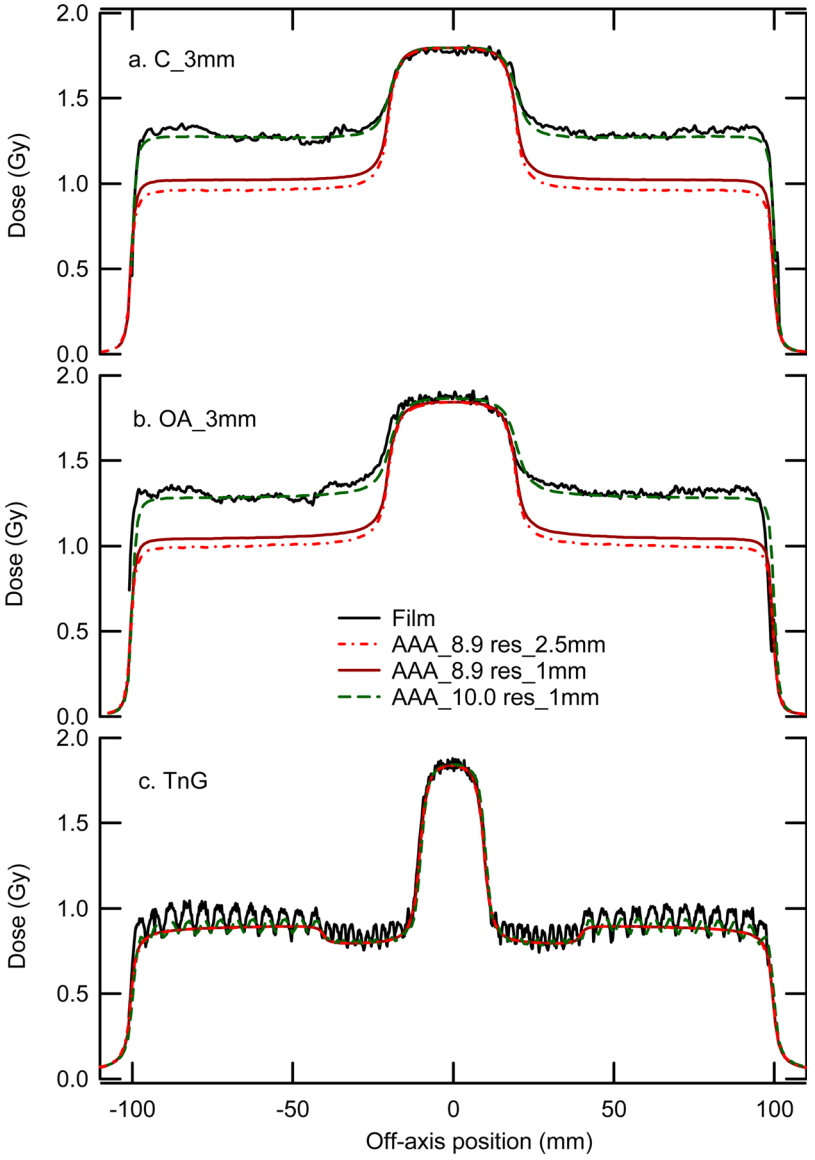


FIG. 7. Effect of the resolution on the calculation accuracy: Measured (film) (black line) and calculated doses (AAA 8.9 with 2.5 mm (dotted line) or 1 mm (solid line) resolution and AAA 10.0 (dashed line) with a 0.3 mm fluence resolution and 1 mm dose calculation resolution) for (a) the central DLG test setup with a 3 mm gap between the leaf tips, (b) the off-axis test setup with a 3 mm gap between the leaf tips and (c) the tongue and groove setup.

angular resolution to 1° rectifies the problem and results in good agreement between calculated and measured (film and 2D array) dose levels. Line profiles corresponding to the arc delivery of the highly asynchronous MLC movement are shown in Fig. 8(c): in agreement with the above results on the static gantry tests, the high resolution fluence available to the AAA 10.0 version proves beneficial in the accurate modeling of the tongue and groove patterns. Even so, the 8.9 dose calculation version reports a dose level that corresponds well to the average film dose level and to the absolute dose level measured with the 2D array ($5 \times 5$ mm$^2$ ion chambers).

### *III.B.2. Performance assessment of the RA optimization algorithm*

The artificial structure sets provide interesting insight in the behavior of the PRO8.9. A selection of planning results is listed in Table II for the Millennium120 MLC. When different plans are listed for the same structure set, all of them are obtained with identical constraints and priorities during the optimization process to allow meaningful inter comparison. First, the automatic isocenter position and couch rotation parameter optimization, available at the onset of the RA optimization process was found to be of very limited use as this optimization process does not take possible collisions into account. Second, when requesting an automatic collimator rotation optimization, in all of the observed cases, the collimator was simply rotated over 45°. Although a 45° collimator rotation may present some mechanical advantages (such as a larger maximum field opening in the longitudinal direction), from the obtained plans it can be concluded that this "optimized" collimator rotation is not necessarily the best choice in all cases. An excellent RA plan is obtained for the central cylinder with collimator 0, resulting in a near-perfect coverage of the PTV (LCF = 1) and only 3% of the 95% dose volume situated outside of the PTV. When using the automatic collimator rotation, although the CI is nearly identical to the one obtained for collimator zero plan, the LCF shows that 3% of the PTV is underdosed while the NTOF reports that 7% of the 95% dose deposition is situated

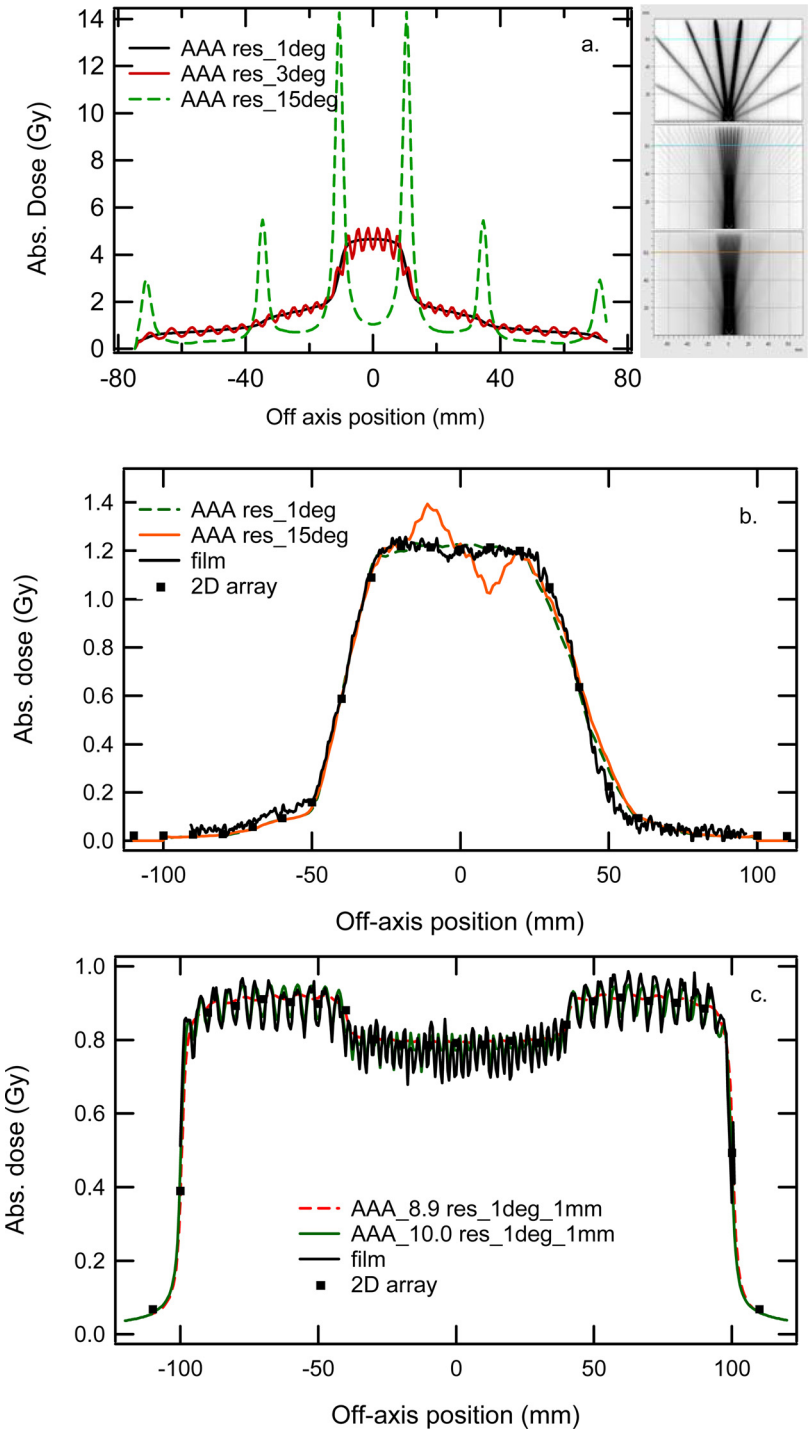


FIG. 8. Effect of the angular resolution on the calculation accuracy: (a) Sunrise test calculated with 15° (dashed line), 3° (solid line) and 1° (solid black line) angular resolution. The position of the extracted line profiles is shown on the 2D dose images displayed on the right of the graph. (b) Dynamic gantry, sweeping gap test results for film (black line), 2D array (black squares), and AAA 8.9 dose calculations with an angular resolution of 15° (solid line) and 1° (dashed line). (c) Line profiles corresponding to the Tongue and groove arc, measured with film (solid black line) and the 2D array (black squares) and calculated with 1° angular resolution and 1 mm dose grid resolution for a 2.5 mm (dashed line) and 0.3 mm (solid line) fluence map resolution.

outside of the PTV. This also illustrates the superiority of the LCF and NTOF over the use of the CI. A similar decrease in plan quality between collimator 0 and collimator 45 is observed for the off-axis cylindrical PTV, the spherical prostate and the oesophagus, reaching extreme proportions for the complex snake-shaped target. For the more concave structures, such as the prostate with seminal vesicles and the horseshoe-shaped head and neck structures, better target coverage and dose homogeneity is obtained with the 45° collimator rotation. For both of these cases, no decent plans (single or double arcs) were obtained with collimator 0. The use of the double arc reduces the hot spots. The disadvantage of using a collimator zero could be the fact that tongue and groove effects of a single leaf pair superimpose into the same transversal plane and are therefore not smeared out during the gantry motion as is the case with a collimator rotation. We have therefore also performed RA optimizations for a much smaller (10°) collimator rotation. Examples are shown for the simple central cylinder and the more complex horseshoe-shaped head and neck case, revealing inferior to extremely poor plan quality, respectively.

From Table II, it can also be concluded that not too much weight should be attributed to the minimum and maximum volume doses as reported by the TPS when evaluating the

TABLE II. Overview of the planning results for a number of RA plans on the artificial structure sets. Different plans listed for the same structure set were all obtained with identical constraints and priorities during the optimization process for meaningful inter comparison. The confirmity Index CI, the lesion coverage fraction, LCF, and the normal tissue overdosage fraction, NTOF, are calculated for the 95% isodose, according to the formulas listed in the manuscript.

| Plan | Dose/fr (Gy) | MU | Collimator (°) | Field size (cm × cm) | $V_{PTV}$ ($cm^3$) | $V_{95}$ ($cm^3$) | $CI_{95}$ | $LCF_{95}$ | $NTOF_{95}$ | $D_{mean}$ PTV(%) | $D_{min}$ PTV(%) | $D_{max}$ PTV(%) | $D_{max}$ 3D(%) |
|---|---|---|---|---|---|---|---|---|---|---|---|---|---|
| CylCentral | 1 | 196 | 0 | 10.9 × 11.5 | 836.3 | 872.6 | 1.040 | 1.00 | 0.03 | 100.0 | 86.7 | 106.7 | 106.7 |
| | | 171 | 10 | 12.4 × 12.5 | | 952.0 | 1.138 | 1.00 | 0.12 | 100.0 | 90.4 | 106.1 | 106.1 |
| | | 163 | 45 | 15.0 × 15.0 | | 865.3 | 1.035 | 0.97 | 0.07 | 100.0 | 87.1 | 107.8 | 107.8 |
| | 10 | 1760 | 45 | 15.0 × 15.0 | | 934.9 | 1.118 | 1.00 | 0.11 | 101.2 | 90.0 | 107.2 | 107.2 |
| Cyl OA | 1 | 200 | 0 | 22.8 × 11.8 | 258.1 | 297.4 | 1.152 | 1.00 | 0.13 | 101.2 | 92.5 | 104.5 | 105 |
| | | | 45 | 22.5 × 22.0 | | 325.8 | 1.262 | 1.00 | 0.21 | 102.1 | 88.7 | 107.1 | 107.1 |
| Prost 3D | 2 | 496 | 0 | 5.7 × 5.6 | 80.2 | 82.6 | 1.030 | 0.99 | 0.02 | 97.5 | 77.6 | 107.5 | 107.5 |
| | | 488 | 45 | 6.4 × 6.4 | | 92.1 | 1.148 | 1.00 | 0.13 | 97.6 | 91.4 | 101.1 | 101.1 |
| Prost SV | 2 | 492 | 0 | 9.0 × 8.7 | 199.2 | 221.4 | 1.111 | 0.92 | 0.19 | 99.6 | 68.4 | 115.5 | 115.5 |
| | | 426 | 45 | 11.9 × 11.9 | | 277.5 | 1.393 | 1.00 | 0.27 | 99.7 | 92.6 | 107.5 | 107.5 |
| | | 320 | 00 | 9.0 × 8.7 | | 248.1 | 1.245 | 0.98 | 0.22 | 99.6 | 70.5 | 117.9 | 117.9 |
| | | 326 | | 9.0×8.7 | | | | | | | | | |
| | | 224 | 45 | 11.9 × 11.9 | | 274.4 | 1.378 | 1.00 | 0.26 | 99.7 | 91 | 104.6 | 105.3 |
| | | 247 | 315 | 11.9 × 11.9 | | | | | | | | | |
| H&N_1PTV | 2 | 329 | 0 | 14.5 × 11.7 | 638.9 | 199.1 | 0.312 | 0.29 | 0.08 | 91.7 | 70.6 | 105 | 105 |
| | | 500 | 45 | 17.0 × 17.6 | | 654.7 | 1.025 | 0.96 | 0.08 | 101 | 82.0 | 111.7 | 111.7 |
| | | 223 | 45 | 17.0 × 17.6 | | 648.4 | 1.015 | 0.97 | 0.05 | 101 | 84.6 | 109.4 | 109.4 |
| | | 264 | 315 | 17.0 × 17.6 | | | | | | | | | |
| | | 174 | 10 | 15.4 × 13.2 | | 238.8 | 0.374 | 0.35 | 0.07 | 92.9 | 78.2 | 104.4 | 104.5 |
| | | 171 | 350 | 15.4 × 13.2 | | | | | | | | | |
| | | 174 | 20 | 15.4 × 13.2 | | 404.9 | 0.634 | 0.62 | 0.03 | 95.9 | 79.0 | 106.8 | 106.8 |
| | | 171 | 340 | 15.4 × 13.2 | | | | | | | | | |
| | | 266 | 30 | 17.0 × 16.3 | | 631.9 | 0.989 | 0.97 | 0.03 | 100.6 | 85.4 | 108.6 | 108.6 |
| | | 236 | 330 | 17.0 × 16.3 | | | | | | | | | |
| | | 231 | 30 | 17.0 × 16.3 | | 642.6 | 1.006 | 0.98 | 0.04 | 100.9 | 84.2 | 107.9 | 107.9 |
| | | 243 | 60 | 15.7 × 17.6 | | | | | | | | | |
| Oesophagus | 2 | 619 | 0 | 15.4 × 20.7 | 119.6 | 151.1 | 1.263 | 1.00 | 0.21 | 101.7 | 88.4 | 106.2 | 106.2 |
| | | 464 | 45 | 20.0 × 20.6 | | 181.7 | 1.519 | 1.00 | 0.34 | 101.4 | 86.1 | 105.4 | 105.4 |
| Snake | 1 | 259 | 0 | 15.2 × 17.1 | 103.6 | 164.1 | 1.584 | 1.00 | 0.36 | 102.1 | 87 | 106 | 106.0 |
| | | 276 | 45 | 16.6 × 17.2 | | 382.8 | 2.694 | 1.00 | 0.73 | 101.3 | 93.5 | 106.3 | 130.8 |
| Lateral Lobe | 2 | 443 | 0 | 10.5 × 5.7 | 38.6 | 46.2 | 1.197 | 0.94 | 0.20 | 100.0 | 79.6 | 105.0 | 105.2 |
| Mediastinum | 2 | 340 | 0 | 10.4 × 5.9 | 61.1 | 70.2 | 1.149 | 1.00 | 0.13 | 100.0 | 91.9 | 102.7 | 102.7 |

quality of a plan. None of the listed RA plans report a minimum dose of 95%, in contradiction to the fact that many of these plans report full PTV coverage by the 95% isodose line. When looking in detail at the dose volume histograms for the plans with LCF equal to unity, one observes that only a negligibly small fraction (typically smaller than 0.3%) of the PTV is actually receiving these lower doses. Similarly, the maximum dose value (PTV or 3D) should be looked at with equal caution and in combination with isodose lines or with percentage volumes of the concerned dose levels. Although this is an already known issue, even in conventional static treatments, its significance increases as plans become more modulated and as the existence of local dose peaks or dips (outside or within the PTV) becomes more probable, as is the case with RA plans.

Both plans obtained on the heterogeneous lung phantom were renormalized to obtain 100% as a mean dose. (The renormalization was small enough not to jeopardize the limits of the actual delivery at the treatment unit.) This renormalization was sufficient to achieve total coverage for the mediastinal volume but left 6% of the lateral lobe volume underdosed. This underdosage could not be overcome by rerunning the optimization with higher penalties attributed to the minimum PTV dose constraint as the dose volume histograms during optimization showed near-perfect coverage already. Both plans are also characterized by relatively large fractions (13 and 20%) of the 95% dose volume situated outside of the PTV.

Very similar plan quality is obtained when optimizing with the Millennium120 MLC or the HD MLC, provided the volumes are not too large to be well covered by the 22 cm maximum MLC field size (in the Y direction, i.e., perpendicular to the leaf movement) of the Novalis TX. For larger volumes, plans optimized on the Novalis TX not only yield inferior target coverage, but also systematically result in unwanted treatment interrupts during delivery. These

interrupts are caused by the fact that a Y1 or Y2 collimator programmed at 11.0 cm can sag to a 11.1 cm position because of gravity during the arc movement. This sagging then exposes the edge of the MLC carriage and therefore results in a treatment interlock. Treatment can be resumed when the collimator is forced back onto its precise 11.0 cm position. To avoid such time consuming interlocks during delivery, if the optimization of the geometric parameters produces a Y1 or Y2 value of 11 cm, we systematically reset it to 10.9 cm before proceeding.

The above conclusions are all obtained with the PRO in the Eclipse 8.9 release. As the optimization modules are still undergoing further development, geometrically simple structures are the ideal candidates to observe changes in the algorithm behavior after software upgrades.

#### *III.B.3. AAA validation of RA plans on artificial structures*

The measurements with the Seven29 in the Octavius phantom confirm that all delivered doses agree with the dose calculations within the predefined acceptance criteria for the gamma evaluation matrix calculated in the VERISOFT software. Very similar results are obtained when using the 2D planar or the 3D dose matrix export. We have requested that at least 95% of all evaluated points have a gamma value smaller than one when using acceptance criteria of 3% local dose difference and 3mm distance to agreement, except in relatively low dose (<0.2 Gy) areas where we allow a 5% dose difference. The lowest dose values (<5% of the maximum dose of the measured data set) are excluded from the evaluation. Figure 9(a) shows a set of line profiles extracted from the overlay between calculation and measurement for four artificial structure plans; the bottom part of the four graphs always shows the ion chamber signal versus the AAA 8.9 calculated profile. The corresponding gamma evaluation images in Fig. 9(b) also indicate the position of the extracted profile within the plane of measurement. The squares represent the position(s) of the ion chambers for which the gamma index exceeds unity. Equally good results were obtained when measuring in the horizontal or vertical plane of the Octavius phantom. The vertical plane allows easy verification of the dose attributed to, e.g., the artificial "spinal cord" cylinder. In addition, subsequent measurements of the same RA treatment plans show near-perfect reproducibility, illustrating both the stability of the measurement and the delivery.

Delta4 measurements (not shown) lead to similar conclusions, confirming the good agreement between calculated and measured dose. For the off-axis cylinder, the Delta4 phantom needed to be moved laterally on the treatment couch because for the central setup, the target volume was partially between the diagonal planes and partially outside of the Delta4 cylindrical phantom. Such a lateral displacement is not easily achieved with high precision as the phantom is difficult to move and no marks on the cylindrical phantom allow easy verification of the lateral shift and the perfect alignment along the longitudinal axis. Results for this laterally displaced setup were inferior to what was observed with the Octavius phantom setup (the latter was measured in the central as well as in the laterally displaced position for comparison).

Line profile comparisons and gamma evaluations on film measurements are also within the predefined acceptance criteria. However, the overall percentage of failed points is larger than in the case of the above mentioned point dose detector systems. This is due to the higher resolution, but also to the higher noise level. As can be seen from the Snake and "Head&Neck" line profile comparisons in Fig. 9(a), narrow peaks visible in the film measurements are smoothened out in the 8.9 dose calculation. In spite of careful calibration curve verification, consecutive film measurements would sometimes show overall absolute dose differences of up to 2%. As the 2D array measurements in Octavius showed near-perfect reproducibility of the delivery, these absolute shifts are attributed to the film measurement procedure and if necessary, film data were renormalized by the appropriate amount (i.e., up to 2%) to obtain the same absolute agreement as observed with the array measurements.

Measurements in the heterogeneous lung phantom setup are shown in Fig. 10. A point dose measurement was again used to confirm (or slightly adjust) the correct absolute dose level of the film. Good agreement was found in both the lateral lobe—protruding into the lung equivalent tissue—and the more central mediastinal case. Although the dose homogeneity in the lateral lobe PTV is inferior to the mediastinal target coverage, at least the reported dose corresponds well to the measured dose, both in the target and lung tissue.

### III.C. Patient QA

#### *III.C.1. Phantom QA*

The patient QA through phantom measurements yields comparable agreement scores to the ones found for the artificial structures on the Octavius phantom for all used methods. The obtained results are also in agreement with what has been reported in literature. The Octavius phantom and Delta4 system require a comparable amount of preparation (i.e., one additional 3D dose calculation, dose export and treatment preparation, amounting to a total of $\sim$20 min/plan) and setup time (5 min. for setting up, 2 min. for performing the cross-calibration or reference dose verification and 5 min. for removing the phantom). The actual measurement takes just about the time needed to deliver the treatment field ($\sim$1 min.). Analysis is most often performed on the spot, allowing instant detection (and correction) of possible errors such as setup or calibration errors. The films turned out to be more tedious to handle and analyze, relatively noisy and less reliable on an absolute level. Both the Octavius and Delta4 setup showed a small ($\sim$1%) systematic deviation when the treatment couch had not been taken into account during the dose calculation but film measurement failed to show this because of the uncertainty in the absolute dose level. All methods showed a decrease in agreement between calculation and measurement when poor values were used for the modeling of the MLC in Eclipse. However, from the comparison between measurement and calculation

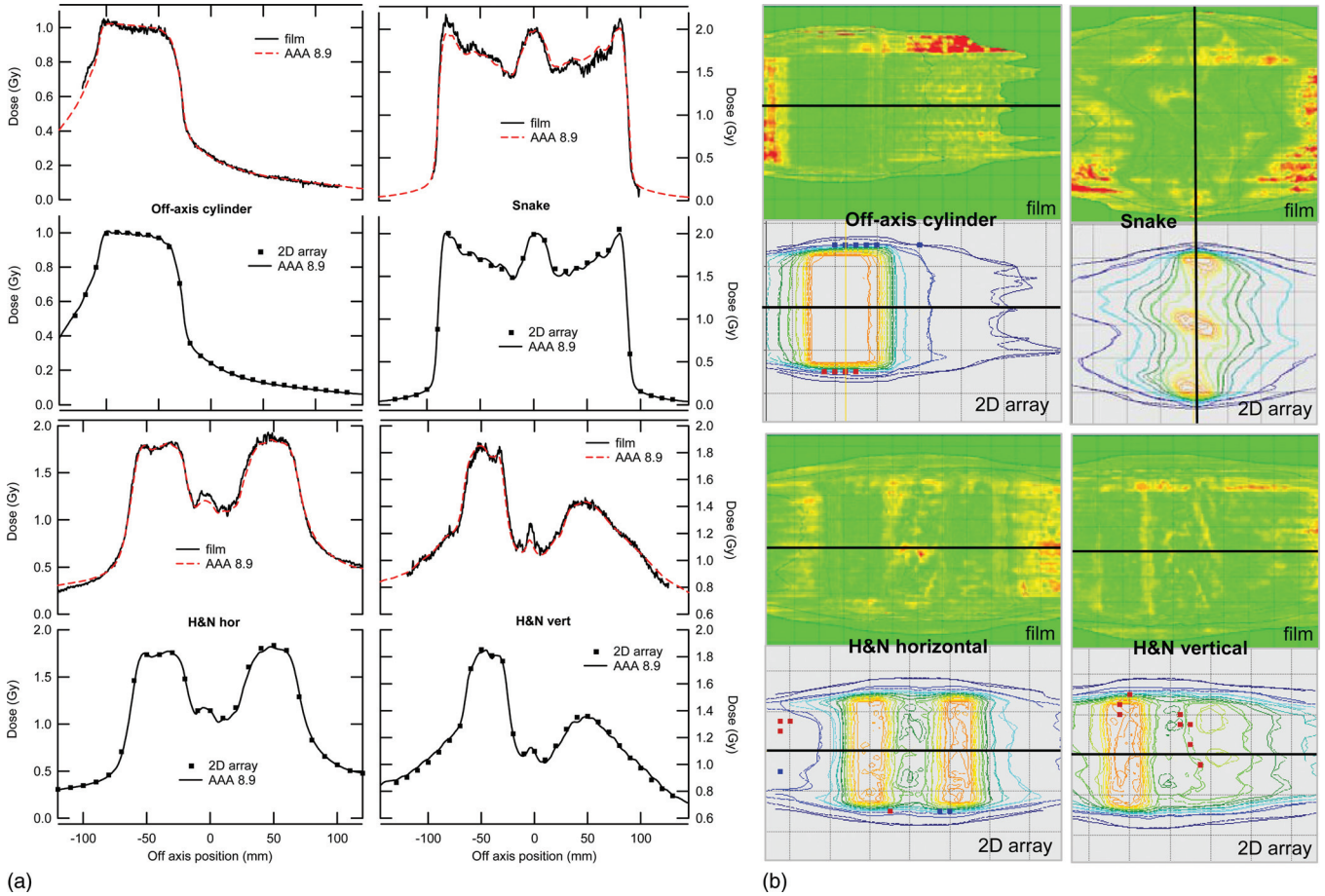


FIG. 9. Examples of a comparison of calculated and measured data for a number of RapidArc plans made on the artificial structures. (a) Line profiles in the upper part of each quadrant show the film data while the lower part displays the 2D array measurement points compared to AAA 8.9. (b) Isodose overlays and gamma evaluation maps from which the line profiles were extracted. Red points indicate measurement points with a gamma value larger than unity. The black lines indicate the position of the lineprofiles shown in (a).

of these clinical plans only, it was not trivial to diagnose the underlying problem.

### III.C.2. Portal dosimetry

The integrated portal dose images obtained with rotating gantry are near-identical to the ones obtained with gantry zero for the same MLC movement and MU delivery and resulted in similar gamma evaluation scores when compared to the calculation (not shown). The differences between both images are so small that it is difficult to assess the origin of the deviation but the sagging of the arm is a known fact and therefore expected to give rise to at least some small deviation. The results show that—for a correctly functioning and calibrated exact arm—the sagging of the arm has no relevant impact on the final outcome of the QA procedure. The time required for the portal dosimetry QA is much shorter than for phantom QA: the preparation of the QA plan takes no more than 1 or 2 min, comparable to the time needed to acquire the dosimetric image and the time spent on the analysis. A total of 10 min per plan is usually more than sufficient.

Figure 11 shows some representative results of the 10.0 Portal Dosimetry solution. The displayed data are obtained from the artificial Snake and Head&Neck plan, in both cases showing one out of the two arcs used per plan. Images obtained on real patient plans yield similar results, albeit on more complex looking images. The gamma distribution was calculated with 3%, 3mm criteria and—adapting previously established acceptance scores for IMRT fields[65] to the new gamma calculation options in the 8.9 software version—requesting 95% of the in-field points to be within these limits. Whereas some images yield near-perfect gamma scores [e.g., Fig. 11(b)] others show small islands or stripes of discrepancies [e.g., Fig. 11(a)] but most of the tested images comply with the above constraints.

## IV. DISCUSSION

Although extendable to other commercially available arc therapy solutions, the described implementation and validation package is specifically adapted to the RA solution from Varian Medical Systems.

A number of publications have already addressed the need for additional machine QA. The most widely used is the aforementioned rotational equivalent of the fence tests.[6] An oscillating sweeping gap test was presented by Bhagwat *et al.*[7] Given the appropriate measurement

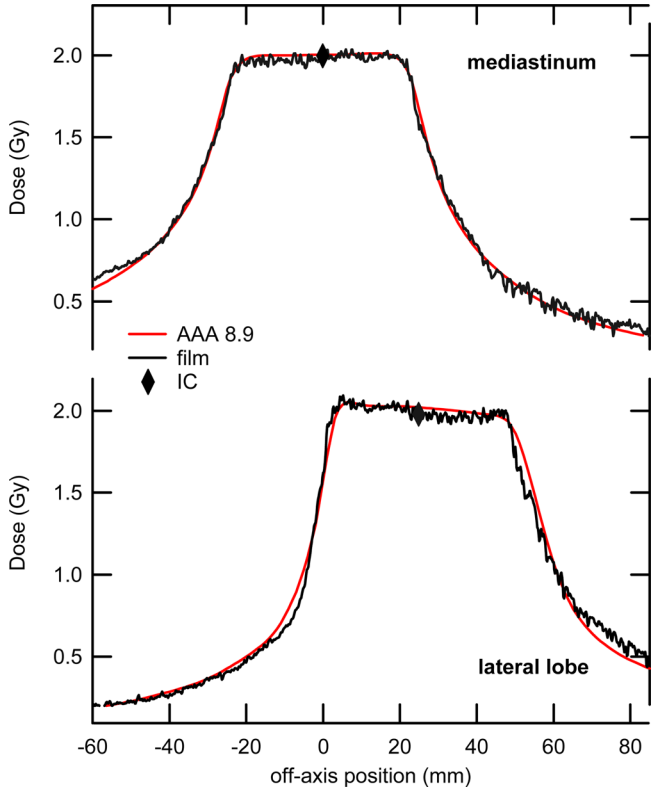


FIG. 10. Measured and calculated data obtained in the heterogeneous lung phantom for the mediastinal and lateral lobe PTV structures. The ion chamber absolute point dose measurement is indicated with a diamond.

equipment, this test is a very practical one, feasible in clinical routine and capable of intercepting some delivery errors (related to gantry angle and leaf positional deviations), but, as described by the authors, it has some limitations, e.g., it does not address all the RA delivery components (e.g., variable gantry speed), and it does not test the treatment delivery to its clinically used limits. The test set we have developed allows a more detailed assessment of all delivery components. Possible problems observed in the dynamic Twinkle can be analyzed through comparison with the static Twinkle results: if both are showing the same deviation from the expected pattern, the problem is to be traced back to the behavior of the gantry as a function of MU, if not, faulty MLC movement could be the culprit. Although the sunrise test was designed to provide feedback on the impact of gravity versus inertia on the gantry angle, it also proved useful in the assessment of the required angular resolution of the dose calculation. In order to be useful in clinical routine, test setups need to be fast and easy to analyze. Although the film setup is fast and easy and simple visual evaluation can already provide useful information, the film is expensive and dosimetric analysis remains a cumbersome aspect. This problem is overcome when using the 2D array (StarCheck or Seven29) in association with an inclinometer: the slightly more time consuming experimental setup is compensated for by the real-time data acquisition and analysis. Unfortunately, the analysis can not yet be performed in the commercially

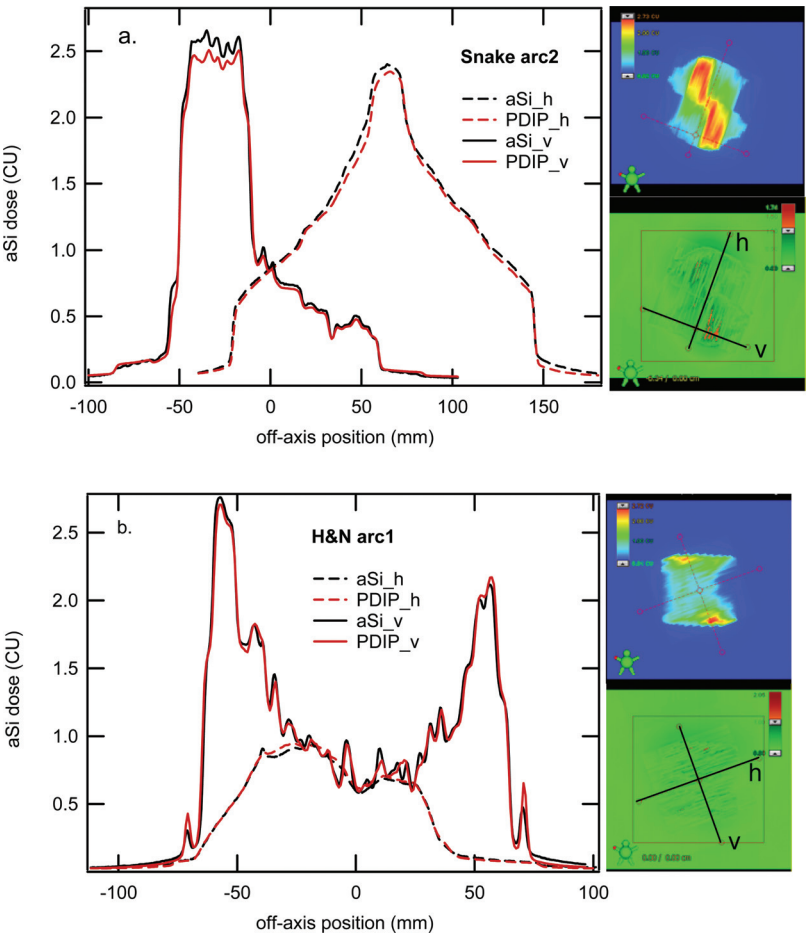


FIG. 11. Examples of the comparison of predicted (PDIP) and measured (aSi) portal dose images for two arc deliveries (on the Novalis TX treatment unit). The position of the displayed line profiles is indicated on the gamma evaluation map. The upper graph shows the area of poor gamma agreement in the "_v" line profile. The lower graph shows the typical extreme modulation observed in the RA integrated images.

available software. Therefore, for routine machine QA, the Snooker Cue test proved to be the most practical of all: its easy experimental setup, on-line (or off-line) assessment and high sensitivity to deviations made it the preferred test to be performed on a regular (weekly) basis in clinical routine. As a disadvantage, this test comprises all delivery components at once and does not allow easy distinction of the source in case of problem detection. Therefore, we have also programmed an additional test for which the MLC movement is not initiated at the latest possible moment in the doseless segment to enforce maximum leaf speed, but rather immediately after beam hold to allow plenty of time for the MLC to reach its next endpoint position before the next batch of MUs is delivered. This test is not used routinely, but kept as an optional additional test to be executed solely in case of problem detection. In addition, possible problems visualized by the Snooker Cue portal images should be further investigated through the use of the static and dynamic Twinkle and the Sunrise test. If no problems are observed; however, the latter tests are only run on a four monthly basis, i.e., after machine maintenance or after a (machine or software) upgrade.

It is advisable to extend validation tests for dose calculation of RA treatments beyond what is advised in standard TPS acceptance recommendations. As shown by our validation tests, MLC parameters as derived according to the standard procedures for IMRT implementation are also adequate for RA treatment dose calculations. To ensure sufficiently accurate dose calculation, users should be careful to define a sufficiently high angular resolution. For most clinical cases, the default control point based angular resolution appears to be adequate, but should by no means be reduced for the purpose of decreasing calculation times. For the AAA 8.9 release, high dose peaks resulting from narrow leaf gaps or tongue and groove effects are smoothened out in the calculated dose matrix. Requesting a dose calculation grid of 1 mm instead of the more commonly used 2.5 mm grid considerable increases the dose calculation time (approximately by a factor 6) but provides only limited gain in dose accuracy. Although one might speculate the discrepancy to be due to suboptimal modeling of the dosimetric leaf gap parameter, the underlying cause is the fixed 2.5 mm resolution of the photon fluence distribution, as can be concluded from much better agreement obtained with the AAA 10.0 release, using identical MLC parameters but a 0.3 mm fluence resolution. In the PRO-generated RA fields, no clinically relevant discrepancies were observed because the above effects are smeared out spatially during the gantry rotation and the continuous MLC movement. (Note that the lower resolution in AAA8.9 merely broadens the peak while leaving its integral dose intact.) Important discrepancies are only expected to be found in plans with extreme modulation, for which it would be advisable to perform a high resolution calculation (1 mm) with AAA10.0.

The geometrically simple, artificial structures make a helpful package to gain experience and understanding in the behavior of the RA optimization algorithm while also providing a transparent RA dose calculation and validation set. For comparing the quality of different plans on the same structures, we found the LCF and the NTOF to be the most useful parameters, in combination with visual isodose evaluation and mindful verification of the global and PTV dose maximum. The strong—sometimes unintuitive—dependence of the plan quality on the collimator rotation should be kept in mind during clinical treatment planning. Site-specific class solutions could provide assistance in selecting the appropriate (initial) collimator rotation(s) for single as well as double arcs and if plan quality is unsatisfactory, one should consider rerunning the optimization for a number of different collimator angles. In addition, as the PRO8.9 internal dose calculation algorithms simplifies the heterogeneity correction according to the Modified Batho model, suboptimal target coverage can be observed in the final AAA dose calculation for e.g., PTVs within or in the proximity of heterogeneous media such as lung tissue. This is not a RA specific problem, but is also observed in the IMRT plans as the IMRT optimization algorithm uses the same internal dose calculation engine as the PRO8.9 during optimization. In contrast to the phantom verification of RA plans created on real patient outlines, the (re)calculated dose distribution is not distorted as the plan is both created and verified on the Octavius (or lung) phantom. This makes the interpretation of the results quite straightforward. Although within the predefined acceptance criteria, our film results are slightly inferior to what others have reported in literature.[59] The main reason for this is the fact that we use local instead of global dose gamma evaluation criteria. In addition, our data are extracted from a single film measurement and not averaged out over two simultaneously acquired films.

For patient QA, in-phantom verification appears to be the only option for now that properly checks the TPS and machine performance. We have successfully used the Octavius and Delta4 system as well as Gafchromic film but have now abandoned film in routine because of its cost, its cumbersome calibration and scanning process and offline analysis and its need for an additional absolute (point) dose verification measurement. If no problems are found, the Octavius and Delta4 are comparably valuable systems for use in routine QA. In case of deviations, however, the Octavius phantom with the 2D array is a more transparant and versatile system, allowing easier problem analysis through e.g different isocenter setups within the phantom or through the straightforward detection of problems with the detector itself (e.g., by means of simple open fields in an orthogonal setup with solid water plates). Although much faster than in-phantom QA, the current portal dosimetry solution does not include any gantry angle information and the final, collapsed images are difficult to interpret. In addition, for multiple arc treatments, portal dose images are predicted and acquired for each arc individually, which further complicates the interpretation. As the RA treatment delivery and dose calculation are still fairly new techniques, we are therefore reluctant to use it as a sole means for patient QA. Phantom verification, even with the newly available solutions specifically designed for arc therapy, remains a time consuming verification method that is difficult to organize on a routine basis in a busy department because of

the required time slots at the Clinac. In order to replace the in-phantom verification, independent point dose calculation for RA treatments could be a helpful asset in verifying the absolute dose calculation part while adding angular information to the portal dose reconstruction could make the portal dosimetry a more complete verification.

In summary, for a radiotherapy department to embark on RA treatment delivery, there is no need to obtain the complete set of dosimetric material used in this study, but it is advisable to have access to sufficient equipment to address every column of Table I with at least one measurement method. Furthermore, for hospitals with limited resources, a compact selection of the performed TPS validation tests by means of a 2D array could suffice to verify the consistency with the herein described results. The EPID can perform its role as a high resolution device. Hence, the implementation of a film dosimetry protocol could be avoided. For machine QA purposes, a visual evaluation of the film is often sufficient. The compact selection of RA implementation tests can be put to additional use for dose recalculation after upgrades.

## V. CONCLUSION

Including a dynamic gantry movement and variable dose rate into the intensity modulated treatment considerably complicates both the delivery and plan optimization process. There exists no doubt that this path forward also requires careful monitoring of all steps involved. Numerous publications have already highlighted this, presenting QA and planning results for the different IMAT solutions currently available. We have tried to present a comprehensive, all-in package for the RapidArc solution, addressing machine QA, validation of the dose calculation, assessment of the treatment plan optimization and patient specific QA in clinical routine.

## ACKNOWLEDGMENTS

The authors would like to thank PTW (Freiburg, Germany) for the fruitful collaboration and for providing dosimetric equipment. 7Sigma also has a research collaboration with Varian Medical Systems. The authors wish to thank Dr. V. Remouchamps for his enthusiastic support and for allowing the necessary time slots at the Novalis TX treatment unit.

[1]C. X. Yu and G. Tang, "Intensity–modulated arc therapy: Principles, technologies and clinical implementation," Phys. Med. Biol. **56**, R31–R54 (2011).
[2]C. Wang, S. Luan, G. Tang, D. Z. Chenand, M. A. Earl, and C. X. Yu, "Arc–modulated radiation therapy (AMRT): A single-arc form of intensity–modulated arc therapy," Phys. Med. Biol. **53**, 6291–6303 (2008).
[3]D. Cao, M. K. N. Afghan, J. Ye, F. Chen, and D.M. Shepard, "A generalized inverse planning tool for volumetric–modulated arc therapy," Phys. Med. Biol. **54**, 6725–6738 (2009).
[4]D. A. Palma, W. F. Verbakel, K. Otto, and S. Senan, "New developments in arc radiation therapy: A review," Cancer Treat Rev. **36**, 393–399 (2010).
[5]S. Webb and D. McQuaid, "Some considerations concerning volume–modulated arc therapy: A stepping stone towards a general theory," Phys. Med. Biol. **54**, 4345–4360 (2009).
[6]C. C. Ling, P. Zhang, Y. Archambault, J. Bocanek, G. Tang, and T. Losasso, "Commissioning and quality assurance of RapidArc radiotherapy delivery system," Int. J. Radiat. Oncol., Biol., Phys. **72**(2), 575–581 (2008).
[7]M. S. Bhagwat, Z. Han, S. K. Ng, and P. Zygmanski, "An oscillating sweeping gap test for VMAT quality assurance," Phys. Med. Biol. **55**, 5029–5044 (2010).
[8]J. L. Bedford and A. P. Warrington, "Commissioning of volumetric modulated arc therapy (VMAT)," Int. J. Radiat. Oncol., Biol., Phys. **73**(2), 537–545, (2009).
[9]A. Fredh, S. Korreman, and P. M. A. Rosenschold, "Automated analysis of images acquired with electronic portal imaging device during delivery of quality assurance plans for inversely optimized arc therapy," Radiother. Oncol. **94**, 195–198 (2010).
[10]K. Otto, "Volumetric modulated arc therapy: IMRT in a single gantry arc," Med. Phys. **35**, 310–317 (2008).
[11]T. Bortfeld and S. Webb, "Single–arc IMRT," Phys. Med. Biol. **54**, N9–N20 (2009).
[12]W. F. A. R. Verbakel, S. Senan, F. J. Lagerwaard, J. P. Cuijpers, and B. J. Slotman, "Comments on "Single–Arc IMRT?"," Phys. Med. Biol. **54**, L31–L34 (2009).
[13]K. Otto, "Letter to the editor on "Single–Arc IMRT?" Phys Med Biol **54**, L37–L41 (2009).
[14]T. Bortfeld and S. Webb, "Reply to 'Comments on 'Single–Arc IMRT?", Phys. Med. Biol. **54**, L35–L36 (2009).
[15]T. Bortfeld and S. Webb, "Reply to 'Letter to the Editor on 'Single-Arc IMRT?"," Phys. Med. Biol. **54**, L43–L44 (2009).
[16]I. Iftimia, E. T. Cirino, L. Xiong, and H. W. Mower, "Quality assurance methodology for Varian RapidArc treatment plans," J. Appl. Clin. Med. Phys. **11**(4), 130–143 (2010).
[17]E. Schreibmann, A. Dhabaan, E. Elder, and T. Fox, "Patient–specific quality assurance method for VMAT treatment delivery," Med. Phys. **36**, 4530–4535 (2009).
[18]D. Wagner and H. Vorwerk, "Two years experience with quality assurance protocol for patient related Rapid Arc treatment plan verification using a two dimensional ionization chamber array," Radiat. Oncol. **6**(21), 1–8 (2011).
[19]S. Ceberg, I. Gagne, H. Gustafsson, J. B. Scherman, S. S. Korreman, F. Kjær-Kristoffersen, M. Hilts, and S. Å. J. Bäck, "RapidArc treatment verification in 3D using polymer gel dosimetry and Monte Carlo simulation," Phys. Med. Biol. **55**, 4885–4898 (2010).
[20]M. Iori, E. Cagni, M. Paiusco, P. Munro, and A. E. Nahum, "Dosimetric verification of IMAT delivery with a conventional EPID system and a commercial portal dose image prediction tool," Med. Phys. **37**, 377–390 (2010).
[21]S. Korreman, J. Medin, and F. Kjær-Kristoffersen, "Dosimetric verification of RapidArc treatment delivery," Acta Oncol. **48**, 185–191 (2009).
[22]G. Nicolini, E. Vanetti, A. Clivio, A. Fogliata, S. Korreman, J. Bocanek, and L. Cozzi, "The GLAaS algorithm for portal dosimetry and quality assurance of RapidArc, an intensity modulated rotational therapy," Radiat. Oncol. **3**(24), 1–10 (2008).
[23]I. M. Gagne,W. Ansbacher, S. Zavgorodni, C. Popescu, and W. A. Beckham, "A monte carlo evaluation of RapidArc dose calculations for oropharynx radiotherapy," Phys. Med. Biol. **53**, 7167–7185, (2008).
[24]K. Bush, R. Townson, and S. Zavgorodni, "Monte Carlo simulation of RapidArc radiotherapy delivery," Phys. Med. Biol. **53**, N359–N370, (2008).
[25]T. Teke, A. M. Bergman, W. Kwa, B. Gill, C. Duzenli, and I. A. Popescu, "Monte Carlo based, patient–specific RapidArc QA using linac log files," Med. Phys. **37**, 116–123, (2010).
[26]R. A. Popple, J. B. Fiveash, I. A. Brezovich, and J. A. Bonner, "RapidArc radiation therapy: First year experience at the university of Alabama at Birmingham," Int. J. Radiat. Oncol., Biol., Phys. **77**(3) 932–941, (2010).
[27]S. Johansen, L. Cozzi, and D. R. Olsen, "A planning comparison of dose patterns in organs at risk and predicted risk for radiation induced malignancy in the contralateral breast following radiation therapy of primary breast using conventional, IMRT and volumetric modulated arc treatment techniques," Acta Oncol. **48**, 495–503, (2009).
[28]L. Cozzi, K. A. Dinshaw, S. K. Shrivastava, U. Mahantshetty, R. Engineer, D. D. Deshpande, S. Jamema, E. Vanetti, A. Clivio, G. Nicolini, and A. Fogliata, "A treatment planning study comparing volumetric arc modulation with RapidArc and fixed field IMRT for cervix uteri radiotherapy," Radiother. Oncol. **89**, 180–191, (2008).
[29]A. Clivio, A. Fogliata, A. Franzetti-Pellanda, G. Nicolini, E. Vanetti, R. Wyttenbach and L. Cozzi, "Volumetric-modulated arc radiotherapy for carcinomas of the anal canal: A treatment planning comparison with fixed field IMRT," Radiother. Oncol. **92**, 118–124, (2009).

[30]E. Vanetti, A. Clivio, G. Nicolini, A. Fogliata, S. Ghosh-Laskar, J. P. Agarwal, R. R. Upreti, A. Budrukkar, V. Murthy, D. D. Deshpande, S. K. Shrivastava, K. A. Dinshaw, and L. Cozzi, "Volumetric modulated arc radiotherapy for carcinomas of the oro–pharynx, hypo–pharynx and larynx: A treatment planning comparison with fixed field IMRT," Radiother. Oncol. **92**, 111–117, (2009).
[31]D. Palma, E. Vollans, K. James, S. Nakano, V. Moiseenko, R. Shaffer, M. McKenzie, J. Morris, and K. Otto, "Volumetric modulated arc therapy (VMAT) for delivery of prostate radiotherapy: Reduction in treatment time and monitor unit requirements compared to intensity modulated radiotherapy," Int. J. Radiat. Oncol., Biol., Phys. **72**(1), S312–S312, (2008).
[32]W. F. A. R. Verbakel, J. P. Cuijpers, D. Hoffmans, M. Bieker, B. J. Slotman and S. Senan, "Volumetric intensity–modulated arc therapy vs. conventional IMRT in head–and–neck cancer: A comparative planning and dosimetric study," Int. J. Radiat. Oncol., Biol., Phys. **74**(1), 252–259, (2009).
[33]F. J. Lagerwaard, O. W. M. Meijer, E. A. P. V. D. Hoorn, W. F. A. R. Verbakel, B. J. Slotman, and S. Senan, "Volumetric modulated arc radiotherapy for vestibular schwannomas," Int. J. Radiat. Oncol., Biol., Phys. **74**, 610–615, (2009).
[34]D. Wagner, H. Christiansen, H. Wolff, and H. Vorwerk, "Radiotherapy ofmalignant gliomas: Comparison of volumetric single arc technique (RapidArc), dynamic intensity–modulated technique and 3D conformal technique," Radiother. Oncol. **93**, 593–596, (2009).
[35]B. Aydogan,M. Yeginer, G. O. Kavak, J. Fan, J. A. Radosevich, and K. Gwe-Ya, "Total marrow irradiation with RapidArc volumetric arc therapy," Int. J. Radiat. Oncol., Biol., Phys. **36**(3), 317–320, (2011).
[36]F. Kjær-Kristoffersen, L. Ohlhues, J. Medin, and S. Korreman, "RapidArc volumetric modulated therapy planning for prostate cancer patients," Acta Oncol. **48**, 227–232, (2009).
[37]R. Shaffer, W. J. Morris, V. Moiseenko, M. Welsh, C. Crumley, S. Nakano, M. Schmuland, T. Pickles, and K. Otto, "Volumetric modulated arc therapy and conventional intensity-modulated radiotherapy for simultaneous maximal intraprostatic boost: A planning comparison study," Clin. Oncol. **21**, 410–407, (2009).
[38]S. Vieillot, D. Azria, C. Lemanski, C. L. Moscardo, S. Gourgou, J.-B. Dubois, N. Aill'eres, and P. Fenoglietto, "Plan comparison of volumetricmodulated arc therapy (RapidArc) and conventional intensitymodulated radiation therapy (IMRT) in anal canal cancer," Radiat. Oncol. **5**(92), 1–9, (2010).
[39]A. Fogliata, A. Clivio, G. Nicolini, E. Vanetti, and L. Cozzi, "Intensity modulationwith photons for benign intracranial tumours: A planning comparison of volumetric single arc, helical arc and fixed gantry techniques," Radiother. Oncol. **89**, 254–262, (2009).
[40]A. Fogliata, S. Yartsev, G. Nicolini, A. Clivio, E. Vanetti, R. Wyttenbach, G. Bauman, and L. Cozzi, "On the performances of intensity modulated protons, RapidArc and helical tomotherapy for selected paediatric cases," Radiat. Oncol. **4**: 2, 1–19, (2009).
[41]J. Cai, J. Yue, R. Mclawhorn, W. Yang, K. Wijesooriya, N. E. Dunlap, K. Sheng, F.-F. Yin, and S. H. Benedict, "Dosimetric comparison of 6 MV and 15 MV single arc rapidarc to helical tomotherapy for the treatment of pancreatic cancer," Med. Dosim. In Press.
[42]V. Jacob,W. Bayer, S. T. Astner, R. Busch, and P. Kneschaurek, "A planning comparison of dynamic IMRT for different collimator leaf thicknesses with helical tomotherapy and RapidArc for prostate and head and neck tumors," Strahlenther Onkol., 1–9, (2010).
[43]U. Mahantshetty, S. Jamema, R. Engineer, D. Deshpande, R. Sarin, A. Fogliata, G. Nicolini, A. Clivio, E. Vanetti, S. Shrivastava, and L. Cozzi, "Whole abdomen radiation therapy in ovarian cancers: A comparison between fixed beam and volumetric arc based intensity modulation," Radiat. Oncol. **5**(106), 1–9, (2010).
[44]Y. Rong, G. Tang, J. S. Welsh, M. M. Mohiuddin, B. Paliwal, and C. X. Yu, "Helical tomotherapy versus single–arc intensity–modulated arc therapy: A collaborative dosimetric comparison between two institutions," Int. J. Radiat. Oncol., Biol., Phys. **81**(1), 284–296, (2011).
[45]T. Wiezorek, T. Brachwitz, D. Georg, E. Blank, I. Fotina, G. Habl, M. Kretschmer, G. Lutters, H. Salz, K. Schubert, D. Wagner, and T. G. Wendt, "Rotational IMRT techniques compared to fixed gantry IMRT and tomotherapy: Multi–institutional planning study for head–and–neck cases," Radiat. Oncol. **6** (20), 1–10, (2011).
[46]A. Fogliata, L. Cozzi, A. Clivio, A. Ibatici, P. Mancosu, P. Navarria, G. Nicolini, A. Santoro, E. Vanetti, and M. Scorsetti, "Preclinical assessment of volumetric modulated arc therapy for total marrow irradiation," Int. J. Radiat. Oncol., Biol., Phys. **80**(2), 628–636, (2011).
[47]N. Hardcastle, W. A. Tom′e, K. Foo, A. Miller, M. Carolan, and P. Metcalfe, "Comparison of prostate IMRT and VMAT biologically optimised treatment plans," Med. Dosim. **36**(3), 292–298, (2011).
[48]M. Mehta, P. Hoban, and T. R. Mackie, "Commissioning and quality assurance of RapidArc radiotherapy delivery system: In regard to Ling *et al.* (Int. J. Radiat. Oncol., Biol., Phys. 2008;72;575–581): Absence of data does not constitute proof; the proof is in tasting the pudding," Int. J. Radiat. Oncol., Biol., Phys. **75**(1), 4–6, (2009).
[49]R. Mohan, "Dueling technologies: In regard to Ling *et al.* (Int J Radiat Oncol Biol Phys 2008;72:575–581)," Int. J. Radiat. Oncol., Biol., Phys. **75**(1), 6–7, (2009).
[50]G. Nicolini, A. Clivio, L. Cozzi, A. Fogliata, and E. Vanetti, "On the impact of dose rate variation upon RapidArc implementation of volumetric modulated arc therapy," Med. Phys. **38**, 264–271, (2011).
[51]M. Oliver, I. Gagne, K. Bush, S. Zavgorodni, W. Ansbacher, and W. Beckham, "Clinical significance of multi–leaf collimator positional errors for volumetric modulated arc therapy," Radiother. Oncol. **97**, 554–560, (2010).
[52]L. Tillikainen, H. Helminen, T. Torsti, S. Siljamäki, J. Alakuijala, J. Pyyry, and W. Ulmer. 2008. "A 3D pencilbeambased superposition algorithm for photon dose calculation in heterogeneous media." Phys. Med. Biol. **53**(14), 3821–3839, (2008)
[53]A. Van Esch, L. Tillikainen, J. Pyykkonen, M. Tenhunen, H. Helminen, S. Siljamäki, J. Alakuijala, M. Paiusco, M. Lori, and D. P. Huyskens, "Testing of the analytical anisotropic algorithm for photon dose calculation," Med. Phys. **33**, 4130–4148 (2006).
[54]A. Fogliata, G. Nicolini, E. Vanetti, A. Clivio, and L. Cozzi, "Dosimetric validation of the anisotropic analytical algorithm for photon dose calculation: fundamental characterization in water," Phys. Med. Biol. **51**, 1421–1438 (2006).
[55]A. Van Esch, J. Bohsung, P. Sorvari, M. Tenhunen, M. Paiusco, M. Iori, P. Engström, H. Nyström, and D. P. Huyskens, "Acceptance tests and quality control_QC_ procedures for the clinical implementation of IMRT using inverse planning and the sliding window technique: experience from five radiotherapy departments," Radiother. Oncol. **65**, 53–70 (2002).
[56]C. Chui, S Spirou and T. LoSasso, "Testing of dynamic multileaf collimation," Med. Phys. **23**(5):635–641, (1996).
[57]R. O. Ottosson, A. Karlsson and C.F. Behrens, "Pareto front analysis of 6 and 15 MV dynamic IMRT for lung cancer using pencil beam, AAA and Monte Carlo," Phys. Med. Biol. **55**, 4521–4533 (2010).
[58]L. Feuvret, G. Noël, J. Mazeron and P. Bey, "Conformity index: a review," Int. J. Radiat. Oncol., Biol., Phys. **64**(2), 333–342, (2006).
[59]L. J. van Battum, D. Hoffmans, H. Piersma, and S. Heukelom, "Accurate dosimetry with GafChromic EBT film of a 6 MV photon beam in water: what level is achievable?," Med. Phys. **35**, 704–716 (2008).
[60]A. Van Esch, C. Clermont and M. Devillers, M. Iori and D. P. Huyskens, "On-line quality assurance of rotational radiotherapy treatment delivery by means of a 2D ion chamber array and the Octavius phantom," Med. Phys. **34**(10), 3825–3837 (2007).
[61]D. A. Low, W. B. Harms, M. Sasa, and J. A. Purdy, "A technique for the quantitative evaluation of dose distributions," Med. Phys. **25**, 656–661, (1998).
[62]T. Depuydt, A. Van Esch, and D. P. Huyskens, "A quantitative evaluation of IMRT distributions: refinement and clinical assessment of the gamma evaluation," Radiother. Oncol. **62**, 309–319 (2002).
[63]E. Vanetti, G. Nicolini, A. Clivio, A. Fogliata, and L. Cozzi, "The impact of treatment couch modelling on RapidArc," Phys. Med. Biol. **54**, N157–N166, (2009).
[64]A. Van Esch, T. Depuydt, and D. P. Huyskens, "The use of an a Si-based EPID for routine absolute dosimetric pretreatment verification of dynamic IMRT fields," Radiother. Oncol. **71**, 223–234 (2004).
[65]A. J. Vinall, A. J. Williams,V. E. Currie, A. Van Esch and D. Huyskens, "Practical guidelines for routine intensity-modulated radiotherapy verification: pretreatment verification with portal dosimetry and treatment verification with in vivo dosimetry," Br. J. Radiol. **83**, 949–957, (2010).